

# *In situ* high-temperature 3D imaging of the damage evolution in a SiC nuclear fuel cladding material

Guanjie Yuan<sup>a</sup>, J. Paul Forna-Kreutzer<sup>a,b</sup>, Peng Xu<sup>c,d</sup>, Sean Gonderman<sup>e</sup>, Christian Deck<sup>e</sup>, Luke Olson<sup>c</sup>, Edward Lahoda<sup>c</sup>, Robert O. Ritchie<sup>f</sup>, Dong Liu<sup>a,\*</sup>

<sup>a</sup>School of Physics, University of Bristol, Bristol, UK

<sup>b</sup>Bristol Composites Institute (ACCIS), University of Bristol, Bristol, UK

<sup>c</sup>Westinghouse Electric Company, Cranberry Township, Churchill, PA, USA

<sup>d</sup>Idaho National Laboratory, Idaho, ID, USA

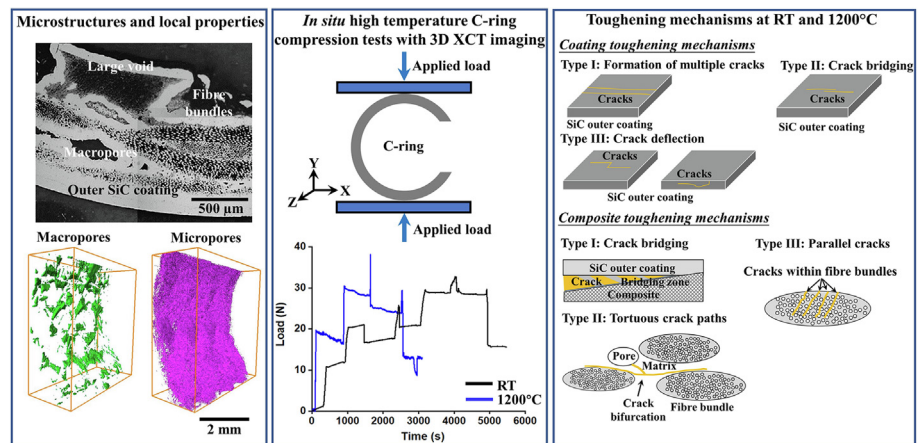
<sup>e</sup>General Atomics, San Diego, CA, USA

<sup>f</sup>Department of Materials Science and Engineering, University of California, Berkeley, CA, USA

## HIGHLIGHTS

- Fracture processes in a coated SiC composite nuclear cladding material were found different at room temperature and 1200 °C.
- At both temperatures, cracking initiated in the outer monolithic SiC coating.
- The stress and strain when first coating crack occurred are much higher at 1200 °C than room temperature.
- Typical crack toughening mechanisms occurred simultaneously in underlying composites upon load drops at both temperatures.

## GRAPHICAL ABSTRACT



## ARTICLE INFO

### Article history:

Received 16 December 2022

Revised 7 February 2023

Accepted 20 February 2023

Available online 21 February 2023

### Keywords:

SiC nuclear fuel cladding  
X-ray computed micro-tomography  
C-ring compression  
Digital volume correlation  
Toughening mechanisms

## ABSTRACT

Silicon carbide (SiC)-based nuclear fission fuel rod cladding has been considered as one of the possible designs for accident tolerant fuels. It is in the form of a SiC fibre reinforced SiC matrix composite tube ( $\text{SiC}_f\text{-SiC}_m$ ) with monolithic SiC outer and/or inner coating layers. This study focuses on the deformation and fracture processes in this material using *in situ* X-ray micro-computed tomography (XCT) at room temperature (RT) and 1200 °C in an inert gas environment in a C-ring compression loading configuration. Prior to testing, local properties and residual stresses were characterised using nanoindentation and Raman spectroscopy since they can impact the mechanical behaviour of the material. The 3D strain distribution, crack formation and propagation processes including the toughening mechanisms (e.g., crack deflection, micro-cracking, crack bridging and bifurcation) are investigated in the coating and underlying composites at RT and 1200 °C. There is no particular sequence which toughening mechanism occurs first – this is very different from the conventional toughening theory in ceramic-matrix composites under uniaxial tension loading. Indeed, no evidence of fibre pull-out or fibre fracture was observed in this  $\text{SiC}_f\text{-SiC}_m$

\* Corresponding author.

E-mail address: [Dong.Liu@bristol.ac.uk](mailto:Dong.Liu@bristol.ac.uk) (D. Liu).

nuclear cladding material in the current C-ring compression configuration. The correlation between local measurements and bulk mechanical behaviour are discussed.

© 2023 The Authors. Published by Elsevier Ltd. This is an open access article under the CC BY-NC-ND license (<http://creativecommons.org/licenses/by-nc-nd/4.0/>).

## 1. Introduction

Due to their excellent irradiation tolerance, high strength and toughness at elevated temperatures [1–5], silicon carbide (SiC) fibre reinforced silicon carbide matrix composites (SiC<sub>f</sub>-SiC<sub>m</sub>) are considered as a promising candidate material for the near-term accident-tolerant fuel (ATF) cladding technology for light water reactors [6–10]. In the ATF cladding design, a layer of monolithic SiC coating is usually applied by chemical vapour deposition (CVD) – tens to hundreds of micrometres thick – to either or both of the outer and inner surfaces of a braided SiC<sub>f</sub>-SiC<sub>m</sub> cladding tube, which then serves as a fission gas barrier [11]. In this work, a Hi-Nicalon™ Type S fibre reinforced SiC<sub>f</sub>-SiC<sub>m</sub> cladding tube material with monolithic SiC outer and inner surface coatings was studied to discern its deformation and fracture behaviour at room temperature (RT) and 1200 °C.

Nuclear-grade SiC<sub>f</sub>-SiC<sub>m</sub> usually consists of highly crystalline, near-stoichiometric SiC fibres [12–14], coated with a pyrolytic carbon (PyC) interphase or PyC/SiC multilayer interphase, embedded in a high-crystallinity SiC matrix [12]. There are two primary types of third generation SiC fibres for this application, e.g., Hi-Nicalon™ Type S fibres (NGS Advanced Fibers Co., Ltd, Japan) and Tyranno SA3 (Ube Industries Ltd, Japan) [12–14]. Detailed properties of these two types of fibres can be found in ref. [14]. The former type, Hi-Nicalon™ Type S fibres, are used in the composite studied in current work, and are known for their low oxygen content and near-stoichiometric composition. They are generally produced by curing polycarbosilane (PCS) fibres with electron beam irradiation and pyrolysis. They consist primarily of nano-polycrystalline β-SiC, with small amounts of residual oxygen/carbon (either in the form of SiO<sub>2</sub> and SiOC) on their surface and throughout the fibre [15,16]. The presence of carbon in the fibre is usually measured by Raman spectroscopy [17], with the carbon content, which affects the local properties of the fibre, evaluated by nanoindentation methods [18]. A layer of thin coating is applied to the fibres and designed to facilitate load transfer, crack deflection and fibre sliding (if any) [19,20]. For nuclear applications the fibre coating is most commonly pyrolytic carbon and is deposited using CVD method with a suitable hydrocarbon precursor. For the SiC matrix, reaction sintering, nano-infiltration transient eutectic (NITE) method and chemical vapor infiltration (CVI) are commonly used to produce a high-crystallinity SiC material with minimal presence of second phases to attain improved mechanical performance and irradiation resistance [14,15]. Depending upon the processing methodology, the consequent local properties can vary substantially and, as such, can affect the stiffness, strength and toughness of the resulting composites [21,22].

For such complex material systems, it is challenging to fully understand their deformation and fracture behaviour under extreme service conditions [11,23–27]. There have been a number of studies performed to date although the majority of tests were conducted at room temperature. Rohmer *et al.* [23] carried out hoop and axial tensile tests at room temperature on one type of SiC<sub>f</sub>-SiC<sub>m</sub> cladding tube. Their material was a CVI SiC matrix reinforced by Hi-Nicalon™ type S fibres in a 3D braided form (braiding angle is ±30° between the reinforcement direction and the tube axis). Acoustic emission (AE) was adopted to identify the elastic limit together with digital image correlation (DIC) used to evaluate the surface strains. These authors found marked anisotropy in the

mechanical properties. In the axial direction, the average modulus and strength were respectively 230 GPa and 460 MPa, compared to 160 GPa and 64 MPa in hoop direction; however, the failure strain was much lower in axial direction (0.70 %) than in the hoop direction (1.52 %). In one related work, Shapovalov *et al.* [24] studied a SiC<sub>f</sub>-SiC<sub>m</sub> cladding reinforced by Hi-Nicalon™ type S SiC fibres at room temperature with higher equivalent fibre tow in the axial direction (1.4 times of that in the hoop direction). They employed a variety of testing methods using DIC including elastomeric insert tests, open-end and closed-end burst tests for hoop strength, uniaxial tensile and closed-end burst tests for axial strength. Values of the average ultimate tensile strength (UTS) and failure strain in the axial direction were found to be higher in the uniaxial tensile tests (245 MPa and 0.64 %) than in the closed-end burst tests (135 MPa and 0.04 %). For the hoop direction, elastomeric insert tests showed the highest values for both the UTS and failure strain (449 MPa and 0.82 %), while close-end tests yielded lower values (370 MPa and 0.73 %). Although the fibre tows were reinforced in the axial direction, based on these results, the hoop strength was still found to be higher than the axial direction. It was suggested by Shapovalov *et al.* [24] that the mechanical performance of the cladding materials is not only influenced by the orientation of the fibre reinforcement, but also by the anisotropic nature of the defect distribution. This strongly implies that to provide a comprehensive understanding of the mechanical behaviour of these material systems, it is crucial to employ imaging characterisation methods *in situ*, preferably in 3D, to acquire microstructural information, such as the braiding patterns and distribution of defects/cracks, under load at temperatures.

Another frequently used mechanical testing configuration for SiC<sub>f</sub>-SiC<sub>m</sub> cladding tubes is a C-ring compression setup [25–28], which is a valuable method due to its small specimen requirements and ease of testing. One of the first openly published C-ring compression tests was conducted at room temperature on a Tyranno SA3 fibre reinforced SiC<sub>f</sub>-SiC<sub>m</sub> cladding material in 2014 [26], although without real-time imaging; plug-expansion tests were also performed on the same material. It was demonstrated that C-ring tests produce comparable mechanical strengths to plug-expansion tests, specifically a hoop strength of ~381 MPa (C-ring compression) vs ~406 MPa (plug-expansion) with a consistency within 6 %. One major advantage of the C-ring test method is that it requires no special complex fixturing which significantly simplifies any high temperature test configuration, Shapovalov *et al.* [25] performed *ex situ* C-ring compression tests on a Hi-Nicalon™ Type S fibres reinforced SiC<sub>f</sub>-SiC<sub>m</sub> material in argon (Ar) at temperatures up to 1900 °C. The strength of the samples retained up to 1900 °C, at which temperature a phase transition occurred in SiC from the face-centred cubic β-SiC to hexagonal closed-packed α-SiC. Although more scarce, mechanical testing experiments have been combined with *in situ* X-ray computed micro-tomography (XCT) imaging to enable a direct 3D characterisation of the evolution of damage; these studies tend to provide far greater insights into the nature and effect of the salient damage and failure mechanisms in these materials [27,29–31]. Saucedo-Mora *et al.* [27], for instance, conducted *in situ* C-ring compression tests at room temperature on a SiC<sub>f</sub>-SiC<sub>m</sub> cladding with monolithic outer SiC coating such that fracture initiation could be observed directly. Croom *et al.* [30] used room temperature *in situ* plug-expansion tests on a un-coated SiC<sub>f</sub>-SiC<sub>m</sub> cladding composite sam-

ple, and found that cracks formed preferably at the intersections of the fibre tows and propagated axially to link up tow overlap sites. Digital volume correlation (DVC) analysis was adopted such that the hoop strain was found to vary significantly through the thickness of composite but was highest at fibre tow crossovers ( $\sim 0.35\%$  at 95 % peak load) which led to crack formation.

In summary, it has become increasingly apparent that damage evolution in these cladding materials is highly dependent on the presence and variation of local microstructures and imperfections/defects. Accordingly, real-time monitoring of such microstructural changes is essentially a necessity during mechanical testing for a fuller understanding of the complex behaviour of this class of composites; indeed, this is especially important for characterizing the damage at the elevated temperatures representative of service conditions for further improving the design of such composite materials. In this regard, we note that to date, there have been no such *in situ* high temperature experiments with X-ray computed micro-tomography imaging on these SiC<sub>f</sub>-SiC<sub>m</sub> cladding tubes in the open literature illustrating the novelty of current work.

In current work, a unique device was adopted to allow *in situ* synchrotron X-ray micro-tomography imaging of the damage and fracture in SiC<sub>f</sub>-SiC<sub>m</sub> cladding materials under C-ring compression at temperatures up to 1200 °C. Digital volume correlation analysis was subsequently conducted to identify local 3D strains [31–33]. The as-received material, in terms of local properties and residual stresses, were characterised to support the interpretation of the X-ray tomography observations.

## 2. Experimental procedures

### 2.1. Materials and sample preparation

Hi-Nicalon™ Type S fibre reinforced CVI SiC matrix SiC<sub>f</sub>-SiC<sub>m</sub> cladding tube materials were provided by General Atomic (GA); detailed manufacturing processes can be found in ref. [34]. A schematic of the C-ring compression configuration is shown in Fig. 1. The outer and inner surfaces were both coated with a monolithic SiC layer, produced by CVD methods. The outer radius ( $r_o$ ), inner radius ( $r_i$ ) and wall-thickness ( $t$ ) of the SiC<sub>f</sub>-SiC<sub>m</sub> cladding tube

**Table 1**  
Dimensions of SiC<sub>f</sub>-SiC<sub>m</sub> cladding tube specimens.

	$r_o$ (mm)	$r_i$ (mm)	$t$ (mm)
X-ray tomography imaging	$4.64 \pm 0.16$	$3.74 \pm 0.16$	$0.90 \pm 0.017$
Calliper	$4.77 \pm 0.048$	$3.78 \pm 0.12$	$0.99 \pm 0.078$

materials were measured by both X-ray computed micro-tomography imaging and callipers; values are given in Table 1 and show good consistency. Overall, the wall thickness  $t$  was  $\sim 0.9$ – $1$  mm with  $r_i$  being  $\sim 3.75$  mm and  $r_o \sim 4.70$  mm. The average ratio of  $r_i/r_o$  was approximately 0.80. For sample preparation, a slow speed diamond saw (operating at 230 rpm) was used to extract the specimens from the cladding tube to a C-ring geometry with a width of  $\sim 5$  mm. The cutting process was operated in a CUTLAM®1.1 manual cutting machine with a water-based coolant. The samples were dried in air for more than three days prior to the beamline experiment.

For nanoindentation and Raman measurements, specimens were first cold mounted using a three-part fast-curing resin (Stuers DuroCit 3 [35]), then ground with 220-grit ( $\sim 4$  mins) and 1200-grit ( $\sim 2$  mins) resin bonded diamond grinding disks, and polished with 9  $\mu\text{m}$  (Stuers MD-Dac polishing cloth), 3  $\mu\text{m}$  (MD-Nap polishing cloth) and 1  $\mu\text{m}$  water-based diamond suspensions ( $\sim 3$  mins at 240 rpm for each polishing step), before surface cleaning in water and ethanol. The samples were dried for more than three days prior to characterisation.

### 2.2. Nanoindentation testing

Nanoindentation tests were performed on the polished cross-sections of as-received SiC<sub>f</sub>-SiC<sub>m</sub> cladding materials using a Hysitron TI Premier nanoindenter with a Berkovich diamond tip. Prior to the measurements, a calibration was conducted on fused silica to provide a tip area function to correct for any geometrical deviations from an ideal Berkovich shape. Polished sample cross-sections were mounted on the loading stage using a thin layer of crystalbond adhesive, and a  $10\times$  objective lens used to identify the location of each indent. Depth control was used during the indentation process with a loading/unloading rate of  $100 \text{ nm s}^{-1}$  and holds at 500 nm indentation depth for 2 s. For areas where multiple indents were performed, indents were placed 10  $\mu\text{m}$  apart. The hardness ( $H$ ) and elastic modulus ( $E$ ) were then calculated using the Oliver and Pharr method [36], from Eqs. (1) and (2), respectively:

$$H = \frac{P_{Max}}{A_r}, \quad (1)$$

$$\frac{1}{E_r} = \frac{1 - \nu_i^2}{E_i} + \frac{1 - \nu_s^2}{E}, \quad (2)$$

where  $P_{Max}$  is the maximum load (mN),  $A_r$  is the projected contact area,  $E_i$  and  $\nu_i$  are respectively the Young's modulus and Poisson's ratio of the tip (1140 GPa and 0.07), and  $E_r$  is the reduced modulus of the sample. A Poisson's ratio  $\nu_s = 0.20$  was used for SiC in the current study [37].

### 2.3. Raman spectroscopy

Raman spectroscopy analysis was conducted on polished cross-sections of the as-received samples to study the SiC phase in the fibre and matrix, and the PyC interphase and residual carbon in the SiC fibre. For polycrystalline SiC, two distinct first-order phonon scattering peaks can be found in the spectrum ( $700$ – $1000 \text{ cm}^{-1}$ ): a transverse optical phonon mode (TO) peak at about

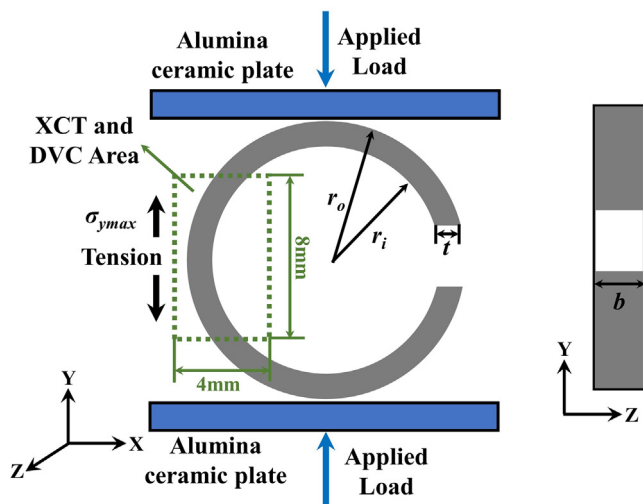


**Fig. 1.** Schematic of the C-ring compression configuration including the coordinate system, specimen dimensions and their definitions. In particular the X-ray tomography scans (marked by dashed green rectangular) were collected at the region of the C-ring with maximum tensile stress/strain. (For interpretation of the references to colour in this figure legend, the reader is referred to the web version of this article.)

797  $\text{cm}^{-1}$  and a longitudinal optical phonon mode (LO) peak at  $\sim 973 \text{ cm}^{-1}$  [38–40]. In general, a compressive stress shifts the Raman peak to a higher wave number, while a tensile stress shifts it to a lower wave number [38]. The stress magnitude ( $\sigma_R$ ) can be estimated by Eq. (3):

$$\sigma_R = |\omega_0 - \omega_s| / \Delta C, \quad (3)$$

where  $\omega_0$  is measured peak position ( $\text{cm}^{-1}$ ),  $\omega_s$  is stress-free peak position ( $\text{cm}^{-1}$ ), and  $\Delta C$  is the stress conversion factor. DiGregorio *et al.* [40] calibrated  $\Delta C$  to be  $3.53 \pm 0.21 \text{ cm}^{-1}/\text{GPa}$  for the TO mode in polycrystalline  $\beta$ -SiC [41]. For PyC and carbon residuals, three distinct peaks can be found in the Raman spectrum ( $1200$ – $1800 \text{ cm}^{-1}$ ): disorder mode (D) peak at  $\sim 1360 \text{ cm}^{-1}$ , graphitic mode (G) peak at  $\sim 1584.5 \text{ cm}^{-1}$  and D' peak at  $\sim 1620 \text{ cm}^{-1}$ . The  $\Delta C$  for G peak ( $\sim 1584.5 \text{ cm}^{-1}$ ) was calibrated to be  $10 \text{ cm}^{-1}/\text{GPa}$  by Gouadec *et al.* [42].

A Renishaw Invia Laser Raman spectrometer in standard confocal mode was used in the current work with a 488 nm laser at  $\sim 40 \text{ mW}$  incident power focussed by a long working distance  $50 \times \text{Lecia}$  lens with a  $1.5 \mu\text{m}$  spot. The scan range of all Raman spectra was  $200$ – $2000 \text{ cm}^{-1}$ . For the outer and inner monolithic SiC coatings, a 10 s acquisition time was used; for the PyC interphase and SiC fibre (with excessive carbon) and SiC matrix, the acquisition time was 20 s due to the low SiC peak intensity. Peak fitting was performed in Wire 5.3 analytical software to yield the peak position and Full-Width-at-Half-Maximum (FWHM).

## 2.4. Scanning electron microscopy imaging

Scanning electron microscopy (SEM) images of the polished cross-sections of the as-received specimens were acquired using a Hitachi S3500N variable pressure scanning electron microscope operating at an accelerating voltage of 20 kV, 62  $\mu\text{A}$  current in the back-scattered mode.

## 2.5. In situ C-ring compression with X-ray computed microtomography

### 2.5.1. Experimental setup

In situ C-ring compression with simultaneous synchrotron X-ray computed microtomography (XCT) imaging was carried out on beamline 8.3.2 at the Advanced Light Source (Lawrence Berkeley National Laboratory, USA) using an unique high-temperature environmental testing device, the details of which can be found in refs [43–46]. The geometry of the C-ring sample is shown in Fig. 1. Under an applied compressive load, the maximum hoop stress,  $\sigma_{y\text{max}}$ , can be calculated according to ASTM Standard C1323-16 [47] from the relationship:

$$\sigma_{y\text{max}} = \frac{P_U R}{b t r_o} \left[ \frac{r_o - r_a}{r_a - R} \right], \quad (4)$$

where  $b$  is the specimen width,  $P_U$  is the maximum applied load (peak load); the term  $R$  and the average radius  $r_a$  are defined by Eqs. (5) and (6), respectively:

$$R = \frac{r_o - r_i}{\ln \frac{r_o}{r_i}}, \quad (5)$$

$$r_a = \left( \frac{r_o + r_i}{2} \right), \quad (6)$$

Note that although ASTM C1323-16 suggests that the width of the C-ring sample should not exceed twice the wall-thickness to minimize the variation in circumferential stresses through the sample width [47], the finite element analysis (FEA) performed by Embree *et al.* [48] on various  $b/t$  ratio combinations relaxed this constraint. Their FEA calculation results are tabulated in Table S1 in

the Supplementary Materials. In present work, the  $b/t$  ratios of the samples were between 4 and 5, and this is to reduce the potential influence of the variation between samples to ensure the volume of materials studied is representative. Based on ref. [48], this was calculated to generate a hoop stress of roughly an order of magnitude higher than the axial stress on the outmost surface of the sample.

During the C-ring compression experiments, all samples were monotonically loaded to failure at room temperature and  $1200 \text{ }^\circ\text{C}$  in an Ar atmosphere. Two samples were tested at each temperature; five to eight XCT scans for each sample were collected at different loading steps with a field-of-view (FOV) of  $8 \times 4 \text{ mm}$  focussed to the middle sections of the C-ring samples, marked by dashed line in Fig. 1. A list of the scans at the normalised loading steps (by the peak load of each sample) are tabulated in Table S2 in the Supplementary Materials. During testing, displacement control was used at a speed of  $\sim 0.5 \mu\text{m}$  increments per second. For each sample, a small pre-load ( $\sim 5 \text{ N}$ ) was applied to avoid sample movement during scanning process and used as reference scan for 3D strain analysis. During XCT scans, a white light X-ray beam was used ( $6$ – $43 \text{ keV}$ ) with a PCO Edge  $2 \times \text{CCD}$  detector,  $2560 \times 2560$  pixels, pixel size  $3.25 \times 3.25 \mu\text{m}$ . For each scan, 1969 projections were acquired over a  $180^\circ$  rotation with a 30 ms acquisition time, which took  $\sim 10$  mins. The reconstruction of XCT scans was carried out using a conventional Gridrec algorithm in the TomoPy software; the rotation centre of each scan was individually identified to remove any deformation artefacts. A flat field correction was applied to each scan to reduce the detector fixed-pattern noise. All reconstructed scans were converted to stacks of 32-bit tiff images.

### 2.5.2. Image processing for 3D visualization and digital volume correlation

All reconstructed XCT scans were imported to open-source software ImageJ [49] for image pre-alignment and cropping to remove the background. The contrast of all cropped datasets was adjusted to a fixed dynamic range ( $-4.1$  to  $2.3$ ) and converted to 8-bit. These datasets were saved as raw data files and then imported into the Avizo Lite (software version 2019.4) [50]. For visualization, each scan was down-sampled by a factor of 2 to improve volume renderings and to reduce computational time. The pre-load XCT scan of each sample was selected for manual segmentation and 3D visualization of the macro- and micro-pores using Image Segmentation Module [50]. The porosity were firstly segmented by adjusting the threshold of masked voxels ( $\sim 7$  to  $\sim 150$ ) [31], followed by a three-time iteration in the Median Filter Module [50] to separate macropores and micropores. The detailed segmentation procedure is shown in Fig. S1.

For Digital Volume Correlation analysis, the datasets were firstly aligned by the Image Registration Module [50] with the pre-load scan to remove rigid body displacement. The datasets were then cropped to the same dimensions ( $5213 \times 2700 \times 4913 \mu\text{m}^3$ ), and imported to the XdigitalVolumeCorrelation Module [50]. The local digital volume correlation method (LA-DVC) was used in current study where the 3D XCT datasets are divided into sub-volumes that are independently correlated. A detailed description of the local DVC method can be found in ref. [33]. A multipass approach [50,51] has been employed where the sub-volume size was decreased stepwise and the displacement calculated from previous pass was fed to in subsequent pass. The uncertainty and error in the digital volume correlation method was assessed by performing 3D sensitivity study, following the procedure in ref. [33]. Reducing sub-volume size from  $208 \times 208 \times 208$  voxels (step 1) to  $104 \times 104 \times 104$  voxels (step 2) and then  $78 \times 78 \times 78$  voxels (step 3) with 0 % overlapping, the calculated strain uncertainties in the hoop direction were found to

be less than 0.01 % in all steps: 0.08 % for step 1, 0.05 % for step 2 and 0.02 % for step 3. These setups were therefore adopted for all the DVC analysis of all samples.

### 3. Results

#### 3.1. Microstructure

An example of a typical microstructure of the as-received  $\text{SiC}_f\text{-SiC}_m$  cladding tube is shown in Fig. 2b. A monolithic  $\text{SiC}$  coating can be seen on both outer and inner surfaces of the tube, which will be referred to as 'outer  $\text{SiC}$  coating' and 'inner  $\text{SiC}$  coating' in the text; they were measured to have a thickness of  $\sim 200\ \mu\text{m}$  and  $\sim 120\ \mu\text{m}$ , respectively. Note that the inner  $\text{SiC}$  coating is very torturous and hence it creates large voids at the interface with the composite (Fig. 2a and 2b).

Inside the composites, two main types of pores were found: (i) macropores in the matrix between fibre bundles, and (ii) micropores inside fibre bundles. For all samples tested, these pores have been segmented by the method described in Section 2.5.2, with the macro- and micro-pores of the as-received  $\text{SiC}_f\text{-SiC}_m$  cladding

tube visualised in 3D and examples are respectively shown in Fig. 2c and 2d. As marked in Fig. 2b, most of the macropores were located at the crossovers of the fibre bundles; the relative locations in 3D are reflected in Fig. 2c. The volume fraction of these macropores and micropores inside the composite were estimated to be  $2.56 \pm 0.23\%$  and  $6.13 \pm 0.52\%$ , respectively. The larger voids, caused by the tortuous inner coating at the interface with the composite, were not included in the pore volume calculations. The pore structure/distribution and volume are consistent across all samples tested which indicates the volume studied is representative. This is further evident by the consistent mechanical behaviour in Section 3.4.

#### 3.2. Local mechanical properties

Nanoindentation tests were performed on the polished cross-sections of the outer and inner  $\text{SiC}$  coating layers, the  $\text{SiC}$  fibres, the matrix within fibre bundles and the matrix between fibre bundles. The results are tabulated in Table 2. For both the outer and inner  $\text{SiC}$  coatings, a line-scan of indents,  $10\ \mu\text{m}$  apart, was collected across the thickness of the coating to show that there was

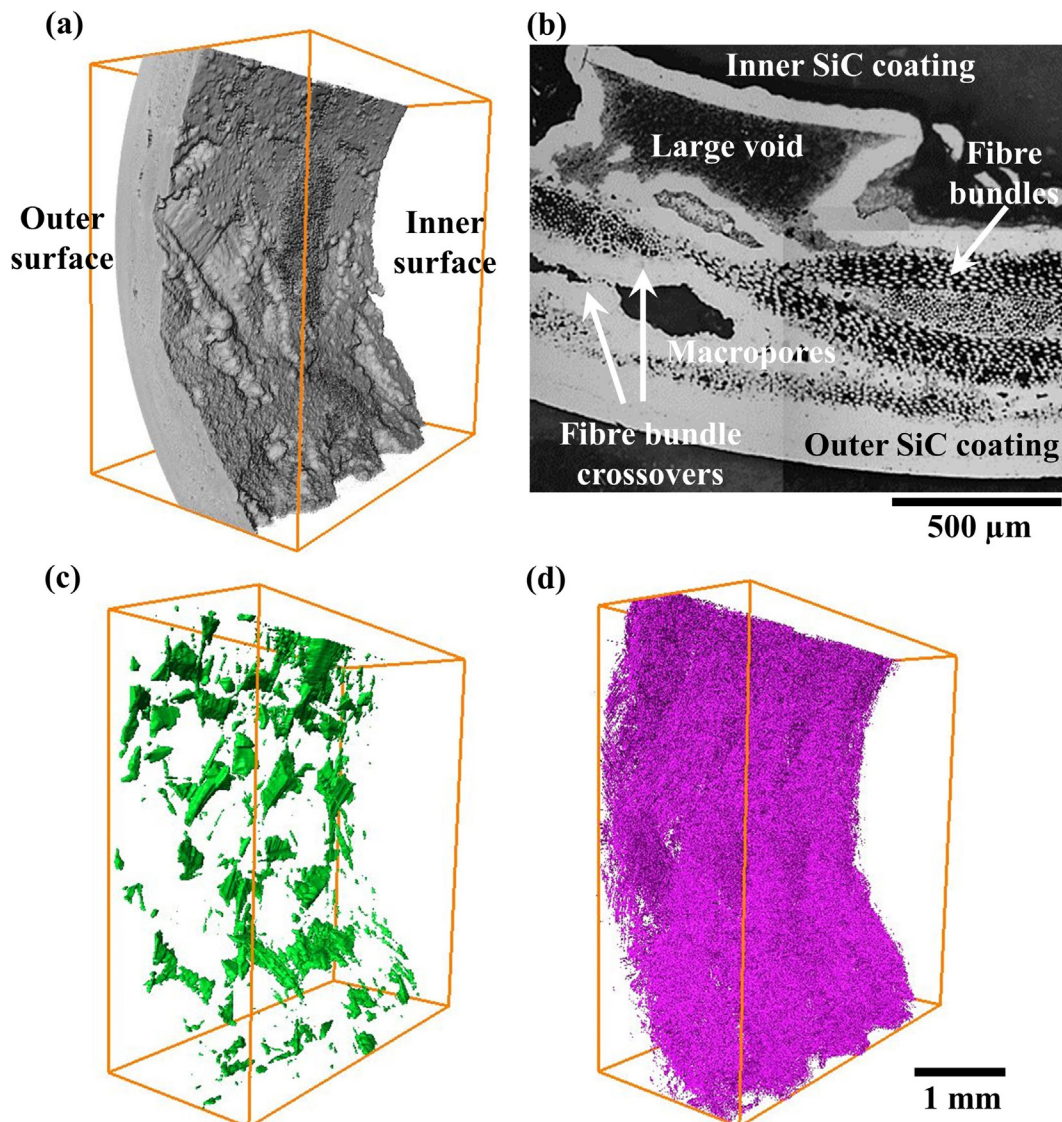


**Fig. 2.** As-received  $\text{SiC}_f\text{-SiC}_m$  cladding tube material: (a) 3D visualization from XCT scans; (b) optical image of the polished cross-section; (c) and (d) are 3D visualization of macro-size and micro-size pores, respectively.

**Table 2**

Measured values of the hardness  $H$  and elastic modulus  $E$  in different areas of the polished cross-section of the as-received SiC<sub>r</sub>-SiC<sub>m</sub> cladding tube material.

Locations	$H$ (GPa)	$E$ (GPa)
Outer SiC coating	31.90 ± 2.26	338.82 ± 5.76
Inner SiC coating	34.68 ± 0.61	340.68 ± 3.29
Fibre	18.69 ± 3.18	174.64 ± 15.60
Matrix within a fibre bundle	33.21 ± 3.13	330.96 ± 9.78
Matrix between fibre bundles	31.99 ± 1.06	310.65 ± 5.03

no obvious difference in the values of hardness,  $H$ , and elastic modulus,  $E$ . Specifically, the outer coating had an average hardness of 31.9 ± 2.3 GPa and an elastic modulus of 338.8 ± 5.8 GPa, whereas for the inner coating the average hardness was 34.7 ± 0.6 GPa with an elastic modulus of 340.7 ± 3.3 GPa, *i.e.*, the outer and inner coatings have very similar properties. For the fibres, a range of indents was performed in different fibre bundles' cross-sections and an average hardness of 18.7 ± 3.2 GPa and elastic modulus of 174.6 ± 15.6 GPa were measured. For the matrix within a fibre bundle, the hardness and modulus were 33.2 ± 3.1 GPa and 331.0 ± 9.8 GPa, but for the matrix between fibre bundles, a slightly lower hardness of 32.0 ± 1.1 GPa and modulus of 310.7 ± 5.0 GPa were measured. Note that the measured hardness and modulus of the fibres were much lower (by about 60 %) than the values for the matrix.

### 3.3. Local residual stresses

Raman spectroscopy has been a frequently utilised technique to measure the residual stresses in SiC and carbon-based materials [17]. Here, the SiC Raman TO peak was used to estimate residual stresses in the outer and inner SiC coatings, SiC fibre and SiC matrix. The carbon G peak was used to measure the residual stresses in the PyC interphase and excess carbon phase in the fibre. Three typical Raman spectra are shown in Fig. S2 in the [Supplementary Materials](#).

Fig. 3a shows the typical microstructure within a fibre bundle with the fibre, thin PyC coating, and micropores in the matrix between fibres. Raman spectra were collected along the radial direction of the fibre at four locations: (1) at the centre of the fibre, (2) at the middle point between the centre and the periphery of the fibre, (3) on the PyC interphase layer, and (4) the matrix adjacent to the fibre. Results are plotted in Fig. 3b. Inside the fibre at locations 1, 2 and 3, both SiC peaks (700–1000 cm<sup>-1</sup>) and carbon peaks (1200–1600 cm<sup>-1</sup>) are apparent, but the carbon peaks are absent in the matrix as there is no carbon.

The Intensity of the SiC TO peaks shows a steady increase from locations 1 to 4 (Fig. 3c). The FWHM of the peak was the lowest at location 1 (the centre of fibre), and approximately half of that at locations 2 and 3. The FWHM of the carbon G band was found to be similar at all three locations inside the fibre, Fig. 3d. The intensity (peak height) ratio of the carbon D and G bands ( $I_D/I_G$ ) has an inverse relationship with the crystallite size when it is over 4.4 nm [52–54], following Eq. (7):

$$L_a = \left(2.4 \times 10^{-10}\right) \lambda_i^4 \left(\frac{I_D}{I_G}\right)^{-1} \quad (7)$$

where  $L_a$  is the crystallite size in nm, and  $\lambda_i$  is the wavelength of the used Raman laser. In the current case, the  $I_D/I_G$  ratio showed a steadily increased from location 1 (1.79) to 3 (2.37).

Values of the tensile residual stresses (listed in Table 3), derived from the SiC TO peak and compared with the reference stress-free peak position, showed a decreasing trend from location 1 (~0.75 GPa) to location 4 (~0.4 GPa), as shown in Fig. 3e. The residual stresses in the excess carbon phase in the fibre, represented by

the G band shift, however, were compressive at the fibre centre at location 1 (around -0.4 GPa) and increased to around -0.6 GPa at the PyC interphase area (location 3) (Fig. 3f). The measurements are compared with literature data in detail in Section 4.2.

### 3.4. Hoop strength at room temperature and 1200 °C

The load-time curves at room temperature and 1200 °C for the C-ring compression tests, with *in situ* XCT imaging, are plotted in Fig. 4. Samples C01 and C02 are tested at RT and samples C03 and C04 are tested at 1200 °C. It can be observed that: (i) the measured behaviour was relatively consistent despite the limited number of samples tested; (ii) during the time periods (~10 mins) that the samples were held at a constant displacement for XCT scanning, continuous load relaxations were observed at 1200 °C tests but not apparent at RT. The load relaxations as a function of applied load are tabulated in Table 4. In general, the amount of load relaxed decreases with increasing applied load. Note the amount of load relaxed during fixed displacement could vary with test configurations, *e.g.*, uniaxial tension or compression could show a different amount.

In addition to load relaxations, there were *load drops* (sudden decrease in load) during the loading process which was found to correspond to the formation of cracks by the X-ray tomography results (see Section 3.5). For RT tests, using sample C01 as an example, the first load drop occurred around 21 N (~0.65  $P_U$ ), as marked in Fig. 4a, followed by the second load drop at ~25 N (~0.70  $P_U$ ), the third load drop at peak load 33.71 N ( $P_U$ ) and a final post-peak load drop at 0.84  $P_U$ . For tests at 1200 °C, using sample C03 as an example, the first such load drop (>10 N), as marked in Fig. 4b, occurred at peak load ( $P_U$ ). This also occurred in similar fashion in sample C04 at 1200 °C. In all samples at both temperatures, the first crack always formed in the outer SiC coating corresponding to the first load drop. The load at which this first coating crack/first load drop occurred was used to derive the outer coating failure strength via Eq. (4), which was ~125–132 MPa at RT and 231–236 MPa at 1200 °C. In other words, these tests consistently showed that a much higher stress is needed to create a first crack in the monolithic SiC coating in the C-ring compression configuration at 1200 °C. Note that after the first coating crack, the stress distribution inside the sample will be modified, such that Eq. (4) may no longer be applicable. However, estimates of the maximum hoop stress have been derived based on this peak load and are listed in Table 5. Note that maximum hoop strength at 1200 °C (~231–236 MPa) is consistently higher than that at room temperature (~200–202 MPa).

### 3.5. Failure processes at room temperature and 1200 °C

The failure processes in the SiC<sub>r</sub>-SiC<sub>m</sub> cladding tube material at RT and 1200 °C were studied by analysing the XCT datasets collected at increasing loading steps on all samples, as respectively shown in Figs. 5–8. The RT and 1200 °C failure modes are described here using samples C01 and C03 as representative examples because the fracture processes in C02 and C04 are similar to C01 and C03, respectively.

At RT, the first load drop accompanies the formation of a surface crack in the outer SiC coating (reached the coating/matrix interface) as shown in Fig. 5a (Crack #1 at 0.52  $P_U$  before peak load) where two XCT slices (Slice 1 and Slice 2) on the X-Y plane were extracted to illustrate this. The first load drop in sample C02 occurred at a very similar load; the calculated outer coating strengths are accordingly consistent at ~125 to 132 MPa, as reported in Section 3.4. A 3D view of this first coating crack is shown in Fig. 6a – it is a continuous crack across the C-ring sample

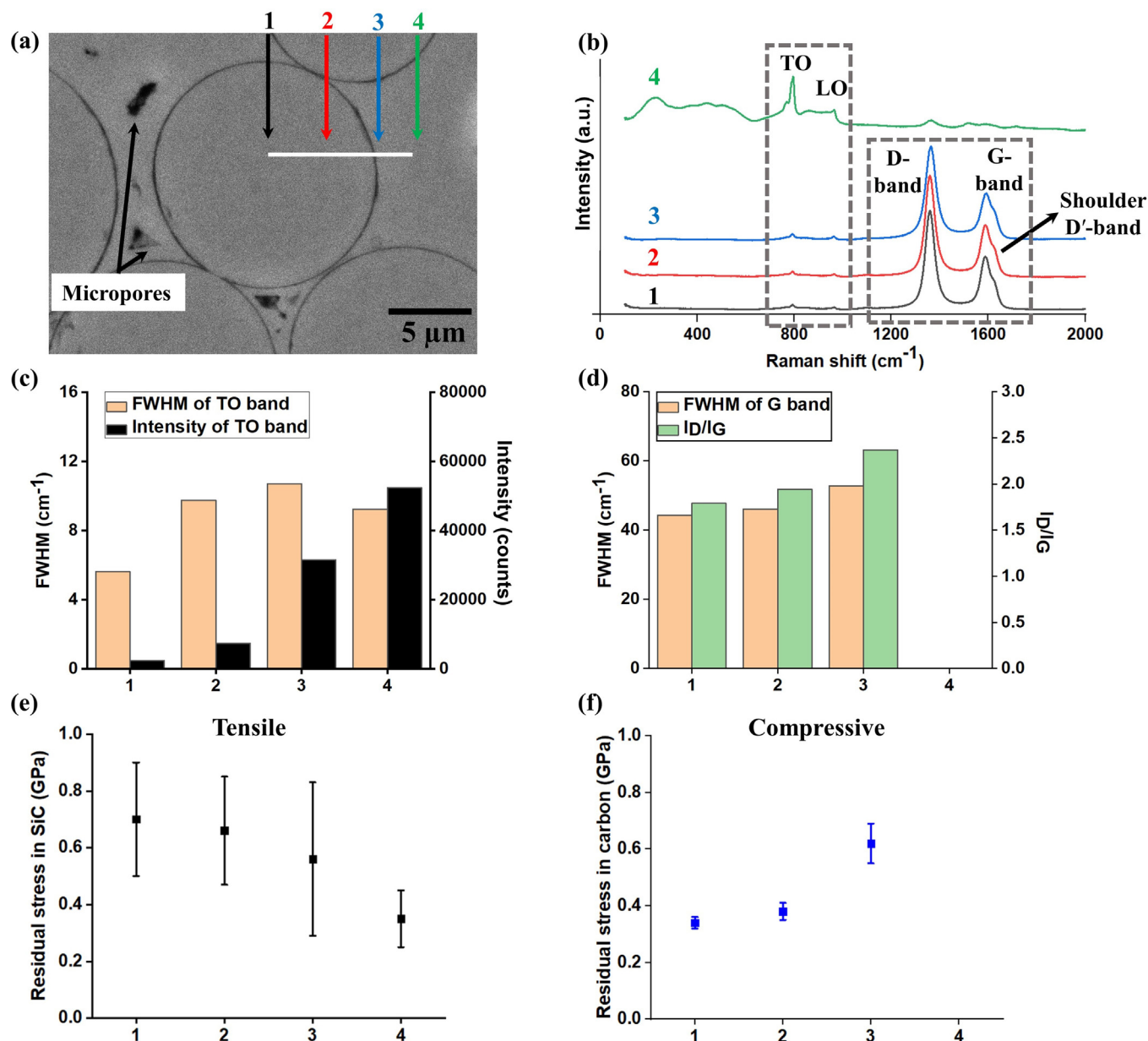


**Fig. 3.** (a) Polished cross-sectional SEM image of one fibre showing the location of four measurements taken on a line scan; (b) Raman spectra of different locations on the polished fibre cross-section: (1) centre of fibre, (2) middle point between the centre and the periphery of the fibre, (3) PyC interphase area and (4) matrix next to the fibre; (c) FWHM and intensities of SiC TO band at locations 1–4; (d) FWHM of carbon G band and  $I_D/I_G$  ratio at locations 1–3; (e) calculated residual stresses in the SiC phase at locations 1–4; (f) calculated residual stresses in carbon phase at locations 1–3.

**Table 3**  
Raman peak positions of the SiC TO band and carbon G band with the corresponding calculated residual stresses ('+' for tensile stress and '-' for compressive stress).

Locations	Raman peak position of TO band (cm <sup>-1</sup> )	Residual stress in SiC (GPa)	Raman peak position of G band (cm <sup>-1</sup> )	Residual stress in carbon (GPa)
Outer SiC coating	795.92 ± 0.43	+0.31 ± 0.13	-	-
Inner SiC coating	796.18 ± 0.42	+0.22 ± 0.12	-	-
Matrix between fibre bundles	795.97 ± 0.35	+0.29 ± 0.10	-	-
Matrix next to fibre	795.77 ± 0.33	+0.35 ± 0.10	-	-
Fibre centre	794.54 ± 0.66	+0.70 ± 0.20	1587.89 ± 0.21	-0.34 ± 0.02
Fibre edge	794.67 ± 0.63	+0.66 ± 0.19	1588.29 ± 0.26	-0.38 ± 0.03
PyC interphase	795.01 ± 0.88	+0.56 ± 0.27	1590.07 ± 0.68	-0.62 ± 0.07

width (*b*) and thickness (*t*). Further loading did not enable the crack to propagate into the underlying composite but rather led to the formation of a second crack (Crack #2) in the outer coating,

Fig. 5b (Slice 3 and Slice 4). This second crack appeared less straight on the coating surface with a discontinuity observed in the 3D segmented image (Fig. 6b); this crack also arrested at the outer coat-

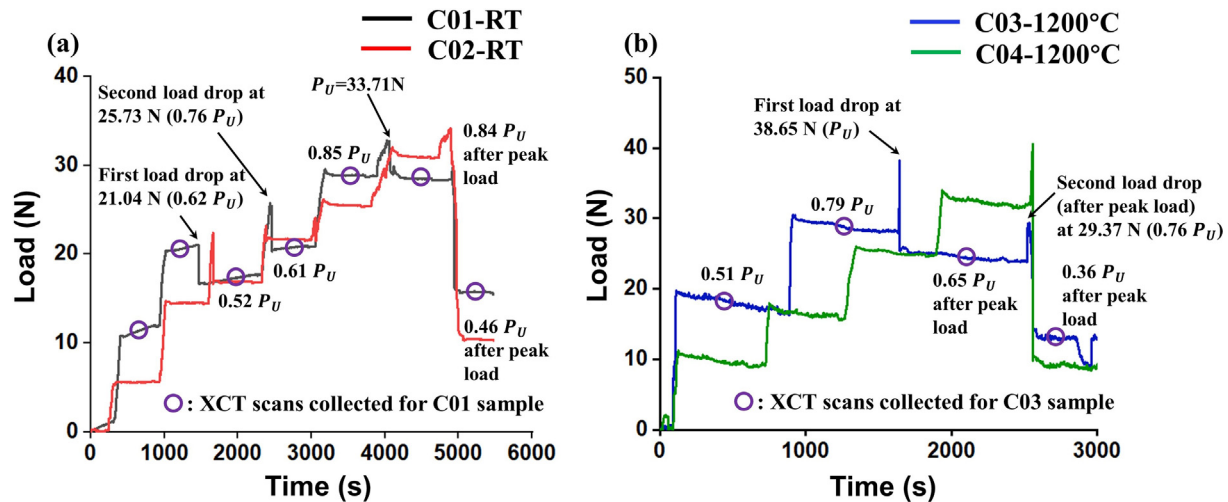


**Fig. 4.** Load-time curves for the C-ring compression tests for (a) samples C01 and C02 tested at RT and (b) samples C03 and C04 tested at 1200 °C. The open circles indicate locations of XCT scans on samples 01 and 03; load drops and peak load ( $P_U$ ) are marked by arrows in C01 and C03 curves.

**Table 4**  
Magnitude of the load relaxation in samples C03 and C04 at 1200 °C at different loading steps.

Specimen	Load before XCT scan (N)	Load after XCT scan (N)	Load relaxation (N)	Percentage of load relaxation (%)
C03	19.75 (0.51 $P_U$ )	16.49 (0.43 $P_U$ )	3.26	16.51
	30.57 (0.79 $P_U$ )	28.25 (0.73 $P_U$ )	2.32	7.59
	25.88 (0.67 $P_U$ )	23.93 (0.62 $P_U$ )	1.95	7.53
C04	11.23 (0.28 $P_U$ )	9.27 (0.23 $P_U$ )	1.96	17.45
	17.91 (0.44 $P_U$ )	15.84 (0.39 $P_U$ )	2.07	11.56
	26.03 (0.64 $P_U$ )	24.67 (0.61 $P_U$ )	1.36	5.22
	33.98 (0.84 $P_U$ )	31.56 (0.78 $P_U$ )	2.42	7.12

**Table 5**  
Calculated coating failure strength and maximum hoop stress at RT and 1200 °C.

Specimen	Sample width (mm)	First load drop (N)	Coating failure strength (MPa)	Peak load (N)	Maximum hoop stress (MPa)
C01-RT	4.85 ± 0.20	21.04	125.07	33.71	200.38
C02-RT	4.86 ± 0.20	22.38	132.76	34.13	202.46
C03-1200 °C	4.81 ± 0.20	Same as peak load	Same as maximum hoop stress	38.65	231.66
C04-1200 °C	4.95 ± 0.20	Same as peak load	Same as maximum hoop stress	40.57	236.29

ing/composite interface, even at the deepest area. Continued loading caused Crack #2 to open in width, connect in the middle section, deflect at the coating/composite interface and propagate deeper into the underlying composite to link up with large matrix pores and interact with fibre bundles, as shown in Fig. 5c (Slices 5–6). These events all occurred before the peak load. With further loading after peak load, Crack #2 penetrated through 80 % (~700 μm) of the thickness of the underlying composite to reach the inner SiC coating (Fig. 5d). The detailed toughening mechanisms active in the composites will be summarised with the high temperature tests (Fig. 9).

At 1200 °C, the XCT scans collected prior to peak load revealed no crack formation (Fig. 7a); the first coating crack formed at a much higher load than at room temperature at the first load drop at peak load (from 38.65 N to 25.65 N for sample C03). Similar to RT, the first crack also occurred in the monolithic SiC outer coating; however, distinct from the straight surface Crack #1 at RT, this first coating crack at 1200 °C was discontinuous with uncracked ligaments and ~90° deflections within the coating along the hoop Y and Z directions of the C-ring sample (see the cross-sectional view in Fig. 7b for Slice 1 and Slice 2 in X-Y plane and X-Z plane). The penetration depth of the crack varies: the majority (~90 %) of the crack length arrested before, or at, the coating/composite interface

due to its shallow depth, or it deflected at the coating/composite interface. About 9.5 % of the total crack length propagated through the coating/composite interface into the fibre bundle in the underlying composite – this crack either stopped inside a fibre bundle by deflection or connected with the matrix macropores (Fig. 7b and Fig. 8).

Although the stress state is clearly modified by the presence of the first coating crack, a final scan after peak load at 0.36  $P_U$  (Fig. 7c) was collected to demonstrate the widening and joining of the discontinuous surface cracks (Fig. 7b). These cracks also propagated deeper into the composite to connect with the macropores (Fig. 7c, Slices 3 and 4).

To summarize, compared to room temperature behaviour, at 1200 °C the first crack formation still occurred within the outer SiC coating but at a much higher load and with a larger load drop (~15–25 N at 1200 °C compared to ~5–6 N at RT). Mechanisms such as uncracked ligament bridging and 90° deflections within the monolithic SiC coating were only observed at 1200 °C. At RT, further loading after the first load drop led to additional smaller load drops associated with more coating cracks prior to peak load. After the peak load, these cracks penetrated deeper into the underlying composite driven by complex stress-state in the C-ring compression configuration. At 1200 °C, as the first load drop coincides

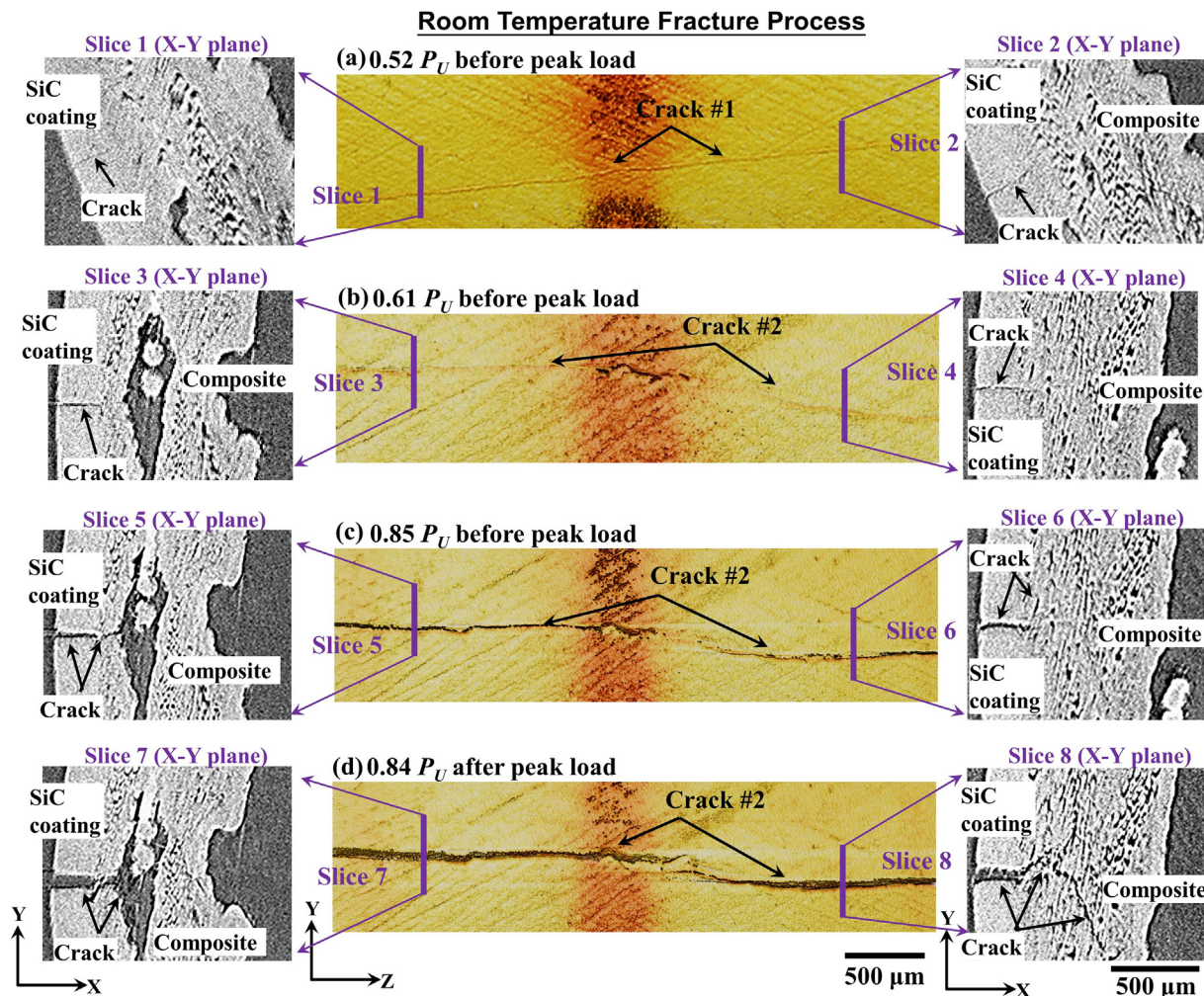


**Fig. 5.** Crack formation and propagation processes at RT illustrated using sample C01: (a) formation of first coating crack (Crack#1) at  $0.52 P_U$  before peak load (crack depth is illustrated by cross-sectional Slices 1 and 2), (b) formation of a second coating crack (Crack#2) at  $0.61 P_U$  before peak load (crack depth is illustrated by cross-sectional Slices 3 and 4), (c) opening of second crack and joining at the middle of the sample at  $0.85 P_U$  before peak load (crack depth is illustrated by cross-sectional Slices 5 and 6); (d) opening of second crack and penetration through the underlying composite reaching the inner SiC coating at  $0.84 P_U$  after peak load (crack depth is illustrated by cross-sectional Slices 7 and 8).

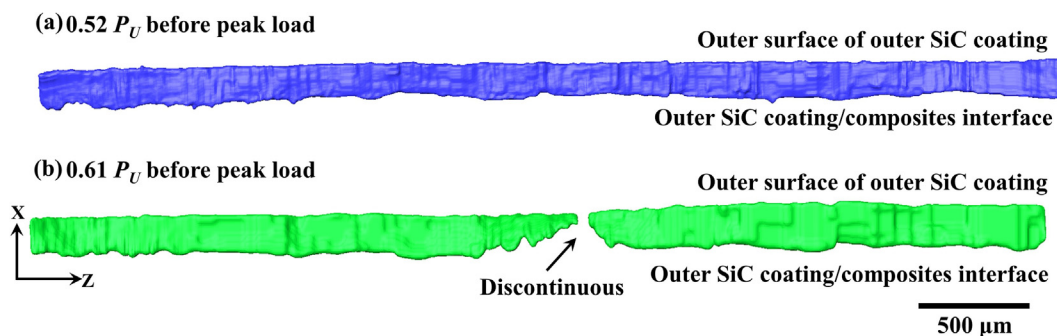


**Fig. 6.** 3D visualizations of the room temperature outer SiC coating surface cracks for sample C01 at (a)  $0.52 P_U$  before peak load with a full-thickness surface crack and (b)  $0.61 P_U$  before peak load with a second surface crack. The colour represents the crack; the discontinuity is uncracked coating material.

with peak load, further loading after the first load drop/peak load also drove the cracks into the composite similar to RT post-peak load behaviour.

At room temperature, toughening in the outer coating was associated with the formation of multiple separate cracks which increased the total crack surfaces/length before peak load (Fig. 9a

Type O-I). At  $1200\text{ }^\circ\text{C}$ , this was achieved by the simultaneous formation of discontinuous cracks separated by uncracked ligament bridges with crack deflection within the monolithic SiC coating (Fig. 9a Type O-II and Type O-III). At both temperatures before peak load, crack deflection at the coating/composite interface was a major mechanism to stop the crack propagating into the underlying

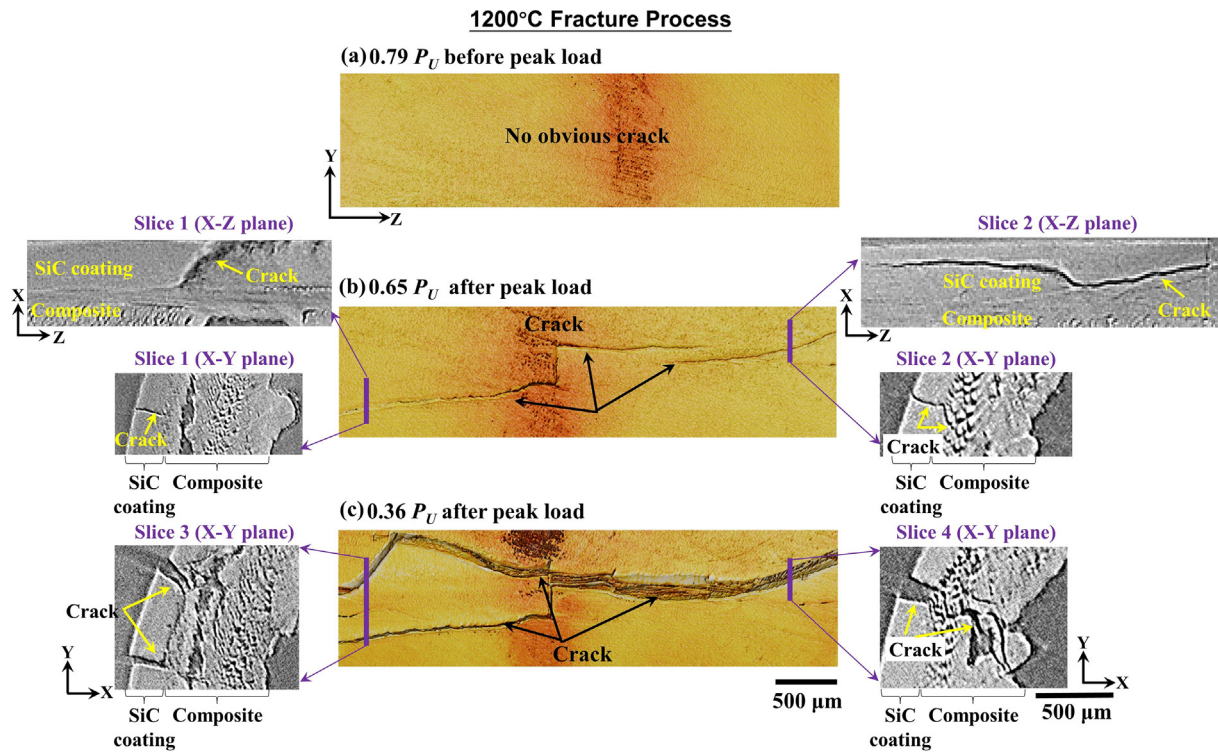


**Fig. 7.** Crack formation and propagation processes at 1200 °C illustrated using sample C03: (a) outer surface of sample at  $0.79 P_U$  before peak load showing no crack formation; (b) formation of first discontinuous coating cracks at  $0.65 P_U$  after peak load showing uncracked ligaments and  $90^\circ$  deflections within the coating (crack deflection either along coating/composite interface or inside coating are shown by cross-sectional Slices 1 and 2 from X-Z plane; crack depth is illustrated by cross-sectional Slices 1 and 2 from X-Y plane); (c) widening and joining of the outer coating crack at  $0.36 P_U$  after peak load, with branching out of a new crack (crack depth is illustrated by cross-sectional Slices 3 and 4 from X-Y plane). The darker orange colour in the middle of the 3D images are artefacts related to the centre of rotation during reconstruction of the datasets. (For interpretation of the references to colour in this figure legend, the reader is referred to the web version of this article.)

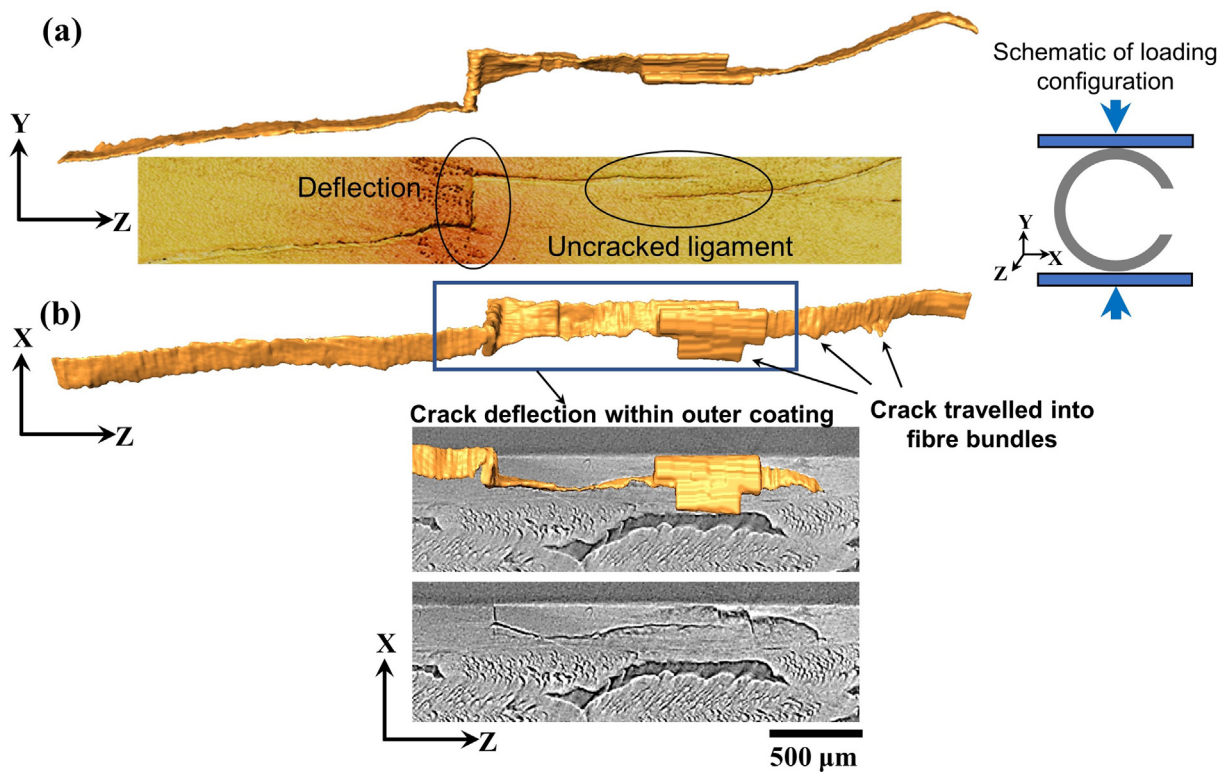
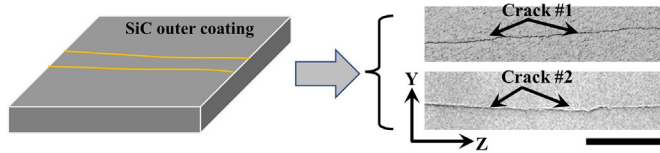


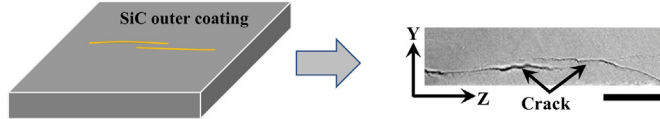
**Fig. 8.** 3D visualization of the outer SiC coating crack of 1200 °C C03 sample at  $0.65 P_U$  after peak load: (a) the YZ view of the crack highlighting features such as crack deflection and uncracked ligament; (b) XZ view of the 3D crack demonstrating the small fraction ( $\sim 9.5\%$ ) of the total crack length that travelled across the coating/composite interface into the fibre bundle, with crack deflection within the SiC coating.

**(a) Coating toughening mechanisms**

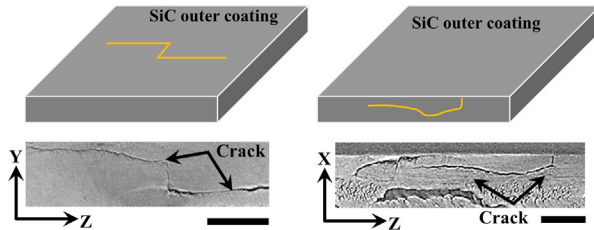
**Type I: Formation of multiple cracks**



**Type II: Crack bridging**

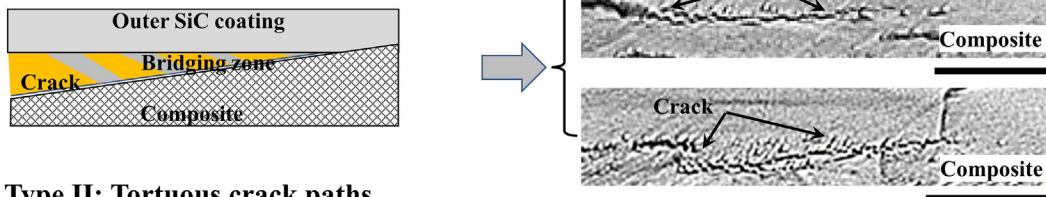


**Type III: Crack deflection**

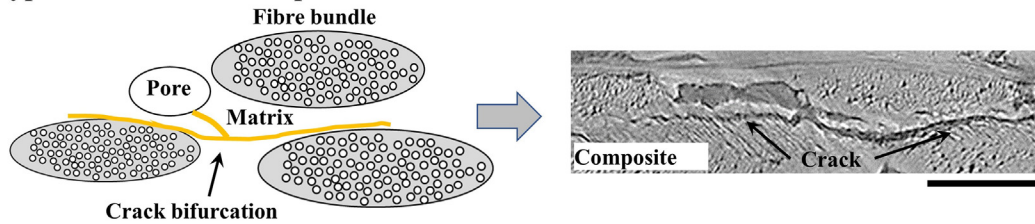


**(b) Composite toughening mechanisms**

**Type I: Crack bridging**



**Type II: Tortuous crack paths**



**Type III: Parallel cracks**

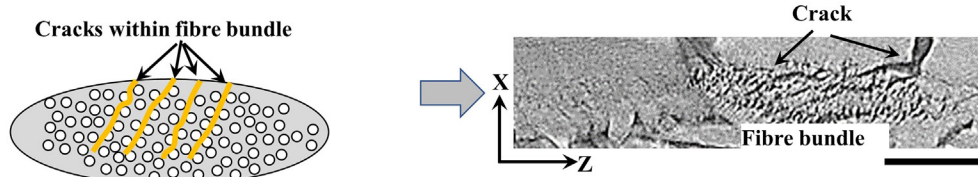


**Fig. 9.** Schematics of the toughening mechanisms for (a) SiC outer coating including Type O-I (formation of multiple cracks), Type O-II (crack bridging) and Type O-III (crack deflection within coating and at coating/composite interface); (b) Composite toughening mechanisms including Type C-I (crack bridging), Type C-II (tortuous crack paths) and Type C-III (parallel cracks) with example XCT slices from Y-Z plane and X-Z plane. All scale bars are 500  $\mu$ m.

ing composite. At the tip of the deflected crack at the coating/composite interface, micro-scale crack bridging was also active as a toughening mechanism (Fig. 9b Type C-I).

Within the underlying composite (primarily after peak load), crack bridging was active at both temperatures primarily within the fibre bundles (Fig. 9b Type C-I). Tortuous crack paths and crack

bifurcation were generated as the cracks linked up with matrix pores and deflected at fibre bundle/matrix interfaces (Fig. 9b Type C-II). Microcracks ahead of a main crack were mostly found to form between fibres within a fibre bundle which acts as a mechanism to diffuse the main crack and arrest its extension (Fig. 9b Type C-III). These observations apply to both room temperature as well as

1200 °C behaviour. It is emphasized that there was no particular order in terms which mechanism occurs first within the composite; these were observed simultaneously upon load drops in all samples investigated. Lastly, no fibre breakage or fibre pull out was observed in the current loading configuration.

### 3.6. Digital volume correlation analysis of 3D local strains

As described in Section 2.5.2, digital volume correlation analysis was used to determine local 3D displacements/strains by correlating deformed XCT datasets to reference scans. Calculated tensile hoop strains,  $\varepsilon_y$ , formed in the coating prior to and after the formation of the first coating crack at both room temperature and 1200 °C, are displayed on the X-Y plane of the C-ring samples in Fig. 10. It is evident that high  $\varepsilon_y$  strain concentration areas already formed inside the outer SiC coating before crack formation at both temperatures (Fig. 10). At room temperature, the XCT scan collected directly before the crack formation in the outer coating, at  $0.62 P_U$  (Fig. 4a), indicated high  $\varepsilon_y$  strains of  $1.88 \pm 0.06 \%$  (Fig. 10a); after the first load drop at  $0.52 P_U$  these strains increased to  $2.10 \pm 0.14 \%$  in the region where the first coating crack initiated (Fig. 10a). At 1200 °C, a  $\varepsilon_y$  strain of  $1.87 \pm 0.12 \%$  was formed at  $0.79 P_U$  in the outer SiC coating (Fig. 10b) prior to the formation of the first coating crack at peak load (Fig. 7); when the load dropped to  $0.65 P_U$  after peak load, the  $\varepsilon_y$  strain increased to  $4.92 \pm 0.13 \%$  (Fig. 10b). The strains at which the first coating crack formed, assuming a linear extrapolation of the measured strains, were found to be  $\sim 1.88 \%$  at RT and  $\sim 2.37 \%$  at 1200 °C.

## 4. Discussion

### 4.1. Local microstructure and properties

The total porosity of the SiC<sub>f</sub>-SiC<sub>m</sub> cladding tube material in the current study was estimated to be  $\sim 9 \%$ , which is broadly consis-

tent with literature results. For instance, values of 10.4 % to 11.1 % were reported for a SiC<sub>f</sub>-SiC<sub>m</sub> cladding tube material with a CVI matrix reinforced with Hi-Nicalon™ type S fibres (3D braided form with a braiding angle of  $\pm 45^\circ$ ) [55], and of  $\sim 5 \%$  and  $\sim 7 \%$  for a French Alternative Energies and Atomic Energy Commission SiC<sub>f</sub>-SiC<sub>m</sub> cladding tube material (with a braiding angle of  $\pm 45^\circ$ ) [27]. Of note is that the diameters and wall thickness of the C-ring samples measured by tomography were found lower than from calliper measurements (Table 1), this can be attributed to the surface roughness of the composites [56].

The overall hardness and modulus of the present SiC fibres (respectively  $\sim 19$  GPa and  $\sim 175$  GPa) were lower than that of the surrounding matrix ( $\sim 33$  GPa and  $\sim 330$  GPa), which is also consistent with literature data. For instance, the indentation hardness and modulus of Hi-Nicalon™ type S fibres in CVI matrix SiC<sub>f</sub>-SiC<sub>m</sub> cladding materials have been reported to be  $\sim 24$  GPa and  $\sim 270$  GPa, compared to respective values of  $\sim 32$  GPa and  $\sim 450$  GPa for the surrounding matrix [57]. Similar nanoindentation testing on Tyranno SA3 fibres in a CVI matrix SiC<sub>f</sub>-SiC<sub>m</sub> cladding yielded an overall fibre hardness of 26–30 GPa and  $\sim 38$  GPa for the surrounding matrices [18]. This was attributed to the presence of carbon inside SiC fibre to lower the hardness and modulus and was verified the hypothesis using the ‘rule of mixtures’ based on the carbon volume fraction estimated from segmentation of fibre cross-sectional images (30 % to 35 %) in their materials [18].

### 4.2. Residual stresses

Residual stresses in the outer SiC coating will affect the strain at where first coating crack takes place. For instance, in tristructural isotropic particle fuel (TRISO), the SiC coating is put under compression to increase its failure strain [58]. The formation of crack or heating to elevated temperatures will subsequently modify the residual stress distribution which impacts the failure strain as well as the overall material’s mechanical behaviour [43]. It is

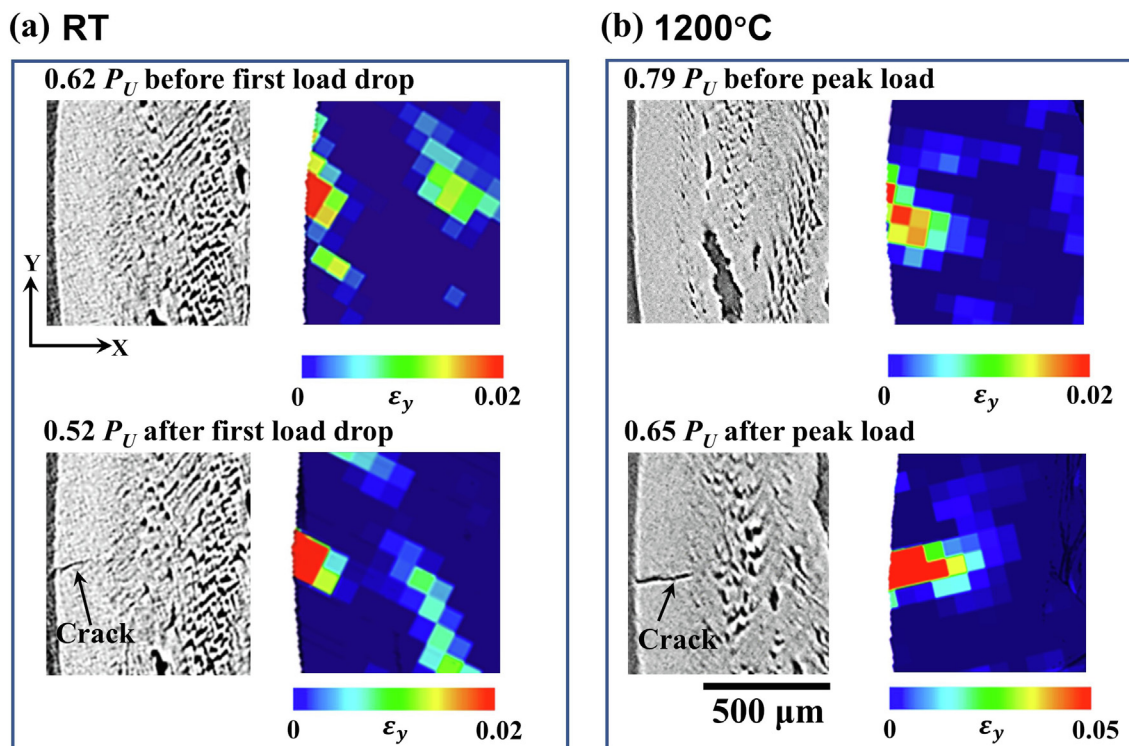


**Fig. 10.** XCT slices and the correspondingly calculated  $\varepsilon_y$  hoop strains in the X-Y plane at different loading steps: for the room temperature sample at (a)  $0.62 P_U$  before first load drop/first coating crack formation, and  $0.52 P_U$  after first load drop; for 1200 °C sample at (b)  $0.79 P_U$  before peak load, and  $0.65 P_U$  after peak load.

therefore critical to conduct a thorough analysis of the distribution of residual stresses in these cladding materials, both when interpreting their deformation and fracture behaviour, and when comparing different types of materials generated by different manufacturing processes.

In this study, SiC was found to have tensile residual stresses in both the outer and inner coatings ( $0.31 \pm 0.13$  GPa and  $0.22 \pm 0.12$  GPa, respectively), in the matrix between fibre bundles ( $0.29 \pm 0.10$  GPa) and in the matrix within a fibre bundle ( $0.35 \pm 0.10$  GPa), as summarized in Fig. 11. As these absolute stress values vary with the reference peak position selected, the relative variation in stress is compared. The stress in the inner coating is  $\sim 0.09$  GPa less tensile than in the outer coating; it is also  $\sim 0.07$  GPa less tensile than in the matrix between fibre bundles. The inference from this data is that the inner coating is under compression in absolute terms to balance out the tensile stresses in the nearby matrix, and that the outer coating could be under tension. This implies that when tested at high temperature (e.g., 1200 °C), the relaxation of this tensile stress will enable the outer SiC coating survive higher failure strains. This could be a potential contribution to the higher failure strain at 1200 °C, as measured by the digital volume correlation analysis in Section 3.6.

Inside individual fibres, the SiC phase has a higher tensile residual stress at the centre of fibre ( $\sim 0.70$  GPa) than at the outer edge ( $\sim 0.56$  GPa) (Fig. 3e). Such a variation across the fibre cross section is not unexpected, as the fibre undergoes complex compositional and microstructural changes during the fibre spinning and heat treatment. Though this is consistent with results in the literature for Raman data collected from a CVD SiC fibre with a tungsten-rich core where the highest tensile residual stress ( $\sim 0.55$  GPa) was measured at the fibre centre [38]. Note that the SiC TO peak has a low FWHM at these high stress areas; as the FWHM is considered to be inversely proportionally to grain size, this implies larger grains at the fibre centre and smaller grains at the edges, again consistent with literature reports [38,39].

Nance *et al.* [17] utilized Raman spectroscopy to measure the residual stresses in the SiC phase inside Hi-Nicalon Type-S SiC fibres at different stages of their manufacture: (i) in the as-received fibre (using a reference stress-free position of  $788 \text{ cm}^{-1}$  which is different from commonly used value of  $797 \text{ cm}^{-1}$ ), (ii) after mechanical braiding of fibre bundles, and (iii) after 33 %, 66 % and 100 % CVI densification processes. These authors reported that processing introduced compressive stresses into the SiC fibres of a magnitude from  $-0.70$  GPa (after mechanical braiding of the fibre bundles) to  $-1.08$  GPa (after the 100 % CVI densification process). Although a different reference peak position was used, their Raman peak position of the SiC TO band ( $\sim 794 \text{ cm}^{-1}$ ) matched well with the band position in current study (Table 3). These and other measurements of the residual stresses of SiC phase in SiC fibres are summarized in Table S3 in the Supplementary Materials.

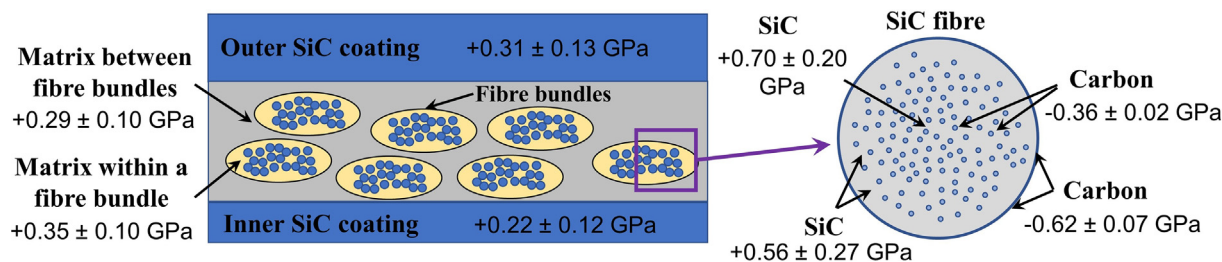


**Fig. 11.** Schematic illustrations of the variation in residual stresses in different components of the SiC<sub>f</sub>-SiC<sub>m</sub> cladding tube material: the outer SiC coating experiences more tensile stress than the inner SiC coating by  $\sim 0.09$  GPa; the matrix within a fibre bundle is  $\sim 0.06$  GPa more tensile than matrix outside a fibre bundle; the residual stresses in this material system, based on SiC phase, have a variation of about 0.13 GPa; within a fibre, SiC phase is under tension while PyC is under compression. The SiC phase in the fibre is under much higher tension (+0.56 to +0.70 GPa) compared with both the inner and outer CVD SiC coatings (+0.22 to +0.31 GPa); ('+' for tensile stress and '-' for compressive stress).

While the SiC phase in the fibre was under highest tensile residual stress, the carbon phase in the fibre was in compression (measured using the G band shift in the Raman spectrum as described in Section 3.3), specifically at a stress of approximately  $-0.36$  GPa at the fibre centre. Using the G band peak position analysis, the PyC interphase area was found to be even more compressive at about  $-0.62$  GPa (Fig. 3f and Fig. 11). This was attributed to volume expansion during processing according to Niu *et al.* [39]. The compressive stress in the carbon phase balances with the tension in the SiC phase. Indeed, compressive stresses in the carbon phase of  $-1.22$  GPa have also been measured at the C-rich boundary between fibre and matrix in SiC/Ni-Cr-Al composites by Raman spectroscopy [39]. Therefore, the data measured in the current work in the SiC fibres are consistent with literature and can be used as input for future constituent materials performance modelling.

The intensity ratio of the Raman D band and G band ( $I_D/I_G$ ) steadily increased from fibre centre to PyC interphase area (Fig. 3d). By using Eq. (7) [53], the carbon crystallite sizes were found decreasing steadily from centre to edge of the fibre (from  $\sim 7.60$  nm to  $\sim 5.74$  nm). In a recent work [17], turbostratic graphite was found inside Hi-Nicalon Type-S SiC fibres (the same fibre type used in this study) by transmission electron microscopy (TEM) images, and grain sizes were reported to be 1 to 4 nm (measured by TEM imaging) - these are in similar range as the Raman spectroscopy measurements although Eq. (7) is no longer valid for crystallite size below 4.4 nm.

#### 4.3. Failure strength/strain at room temperature and 1200 °C

Before detailed discussion of the hoop strength data, it is important to differentiate 'maximum hoop strength' from 'coating failure strength'. The former is used to select the peak load to derive a maximum strength based on Eq. (4) from ASTM Standard C1323-16 [47] which is used by the majority of studies in the open literature data. The latter is to take the load at which the first coating crack occurs to calculate the coating failure stress/strain. In present work, it is suggested that the latter is a more reliable term as the stress-state in C-ring compression will be modified by the onset of first coating crack such that Eq. (4) is likely to be no longer valid.

The room temperature maximum hoop strength of SiC<sub>f</sub>-SiC<sub>m</sub> composite (with and without an outer coating) has been measured by various test methods including C-ring compression, plug-expansion, elastomeric insert, open-end and close-end burst, tensile and compression tests, and found to be similar, specifically in the range of 64 MPa–418 MPa; the corresponding bulk failure hoop strain has been reported to be in the range of 0.19 %–1.52 % [1,4,11,23,24,26,59,60]. A detailed summary of this information is given in Table S4 in the Supplementary Materials. In addition, Saucedo-Mora *et al.* [27] measured 3D local strain in the range of

12–20 % in a coated  $\text{SiC}_f\text{-SiC}_m$  cladding tube using digital volume correlation related to local failure.

In present work, the RT maximum hoop stresses (based on the peak failure load) were  $\sim 200$  MPa, which may be an overestimate of the strength due to deviation from linearity caused by prior crack formation; nevertheless, this value is still within the reported range. The RT coating failure strength was lower at 125–132 MPa, although there are no published data directly reporting the coating failure stress (first load drop) of similar SiC materials under C-ring compression (as far as the authors are aware). However, reviewing the published load/stress-displacement curves for a range of materials, the stresses at first load drop are in the range of  $\sim 180$  to  $\sim 240$  MPa (Table S4 and Fig. S3a and S3b) [11,26]. This range is broadly similar to the current work but the variation in these values can be associated with the differing sample volumes, materials fabrication, overall material stiffness and coating thicknesses.

In general, there are fewer high temperature experiments on tubular  $\text{SiC}_f\text{-SiC}_m$  cladding composites in open literature compared to RT tests; a detailed summary of literature values [1,4,25,60] is given in Table S5. Hironaka et al. (2002) [60] and Nozawa et al. (2014) [1] reported good strength retention of  $\text{SiC}_f\text{-SiC}_m$  compos-

ites at temperatures up to 1200 °C which is consistent with the results of the current work. A notable study in this regard is by Shapovalov et al. [25], where high-temperature C-ring compression tests were performed on two types of Hi-Nicalon™ Type S fibres reinforced  $\text{SiC}_f\text{-SiC}_m$  cladding materials, one with a CVD outer SiC coating ( $\sim 100$   $\mu\text{m}$  in thickness) and tested in air up to 1100 °C, the other without outer SiC coating and tested in air (up to 1100 °C) and Ar environments (up to 1900 °C). For the coated samples, they reported a failure load of  $\sim 16$  N tested at 1100 °C in air. This value is half of the failure load measured in current study at 1200 °C, but the width of their C-ring samples was also half that of the current samples; this implies that the current results are consistent with their measurements. In addition, they found that the peak loads ( $\sim 16$  N) for the coated samples did not decrease at temperatures up to 1100 °C in air, as well as un-overcoated samples up to 1900 °C in Ar ( $\sim 10$  N) [25]; again, this is consistent with the current findings up to 1200 °C.

The retention and/or increase in failure strength is not unexpected; for instance, Gulden [61] reported the fracture strength of dense SiC being approximately constant between room temperature and about 900 °C and then to increase sharply up to the max-

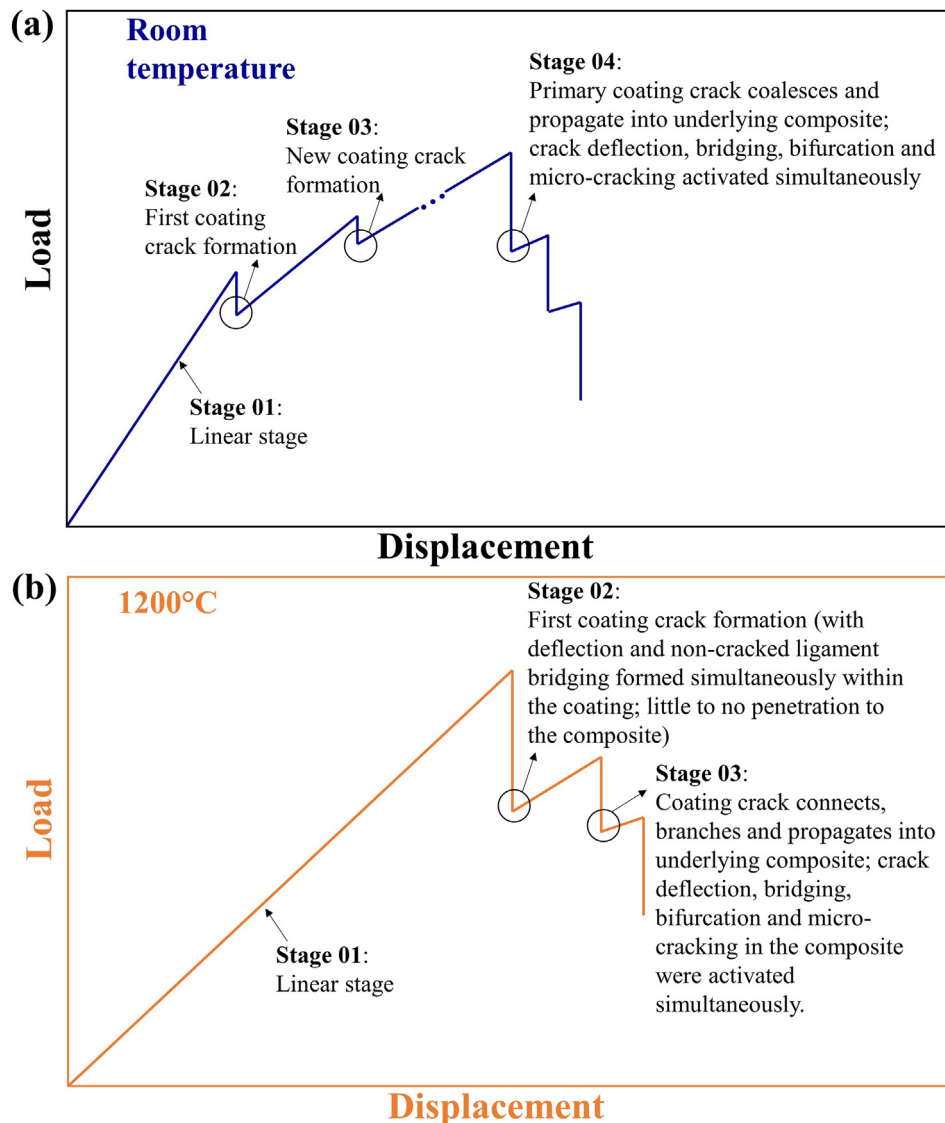


**Fig. 12.** Schematic illustrations of load–displacement curves to display the progressive failure of  $\text{SiC}_f\text{-SiC}_m$  cladding tube materials under C-ring compression at (a) room temperature and (b) 1200 °C.

imum test temperature of 1215 °C to 1400 °C. These imply that the room temperature property tests can be considered as a conservative assessment of the coating failure for such materials systems. However, for accurate modelling of the materials fracture processes, it is noted that the coating failure strength should be differentiated from the maximum peak strength in C-ring compression configuration.

#### 4.4. Failure process and active toughening mechanisms at room temperature and 1200 °C

The documented failure modes of SiC<sub>f</sub>-SiC<sub>m</sub> composites at room temperature are generally considered to occur in three stages [24,26,62]: (i) during the initial linear (elastic) region of the stress–strain curve, the load is shared by both the fibres and matrix with little to no cracks within the material; (ii) at the proportionality limit (akin to the yield strength in a metal), cracks initiated in the matrix propagate along the fibre/matrix interface to result in the nonlinear mid-region of the stress–strain curve (akin to the plastic region in a metal); (iii) with the matrix significantly fractured, load is transferred to the fibres which can lead to fibre pull-out and eventually to fibre fracture, thus correlating with the remainder of the stress–strain curve. However, the real time 3D imaging in the current study suggested very different failure processes (summarised in Fig. 12) in the coated SiC<sub>f</sub>-SiC<sub>m</sub> cladding tubes under C-ring compression. Specifically, (i) the matrix crack was not the first fracture to occur, (ii) several different toughening mechanisms in the coating and composites were activated simultaneously rather than in sequence, and (iii) no fibre fracture/pull out was observed. This suggests that the fracture processes may vary when different loading configurations are applied such as bending, C-ring compression and/or biaxial/triaxial loading; it is inappropriate to presume that the same failure processes in one test configuration will apply to all others. Accordingly, to accurately model material performance, *in situ* testing with 3D imaging on representative samples is essential to identify the specific failure processes for the relevant loading configuration.

In summary, for the current C-ring compression of coated SiC<sub>f</sub>-SiC<sub>m</sub> cladding tubes, at room temperature the failure processes can be classified as follows (Fig. 12a): *Stage 01* - a linear region with no obvious crack formation; *Stage 02* - the first load drop occurs corresponding to crack formation in the outer SiC coating; *Stage 03* - additional crack formation in the coating on further loading (these coating cracks in *Stage 02* and *Stage 03* primarily stay within the coating, either due to their shallow depth or deflection at the coating/composite interface, and do not yet fully propagate to the underlying composite); *Stage 04* - upon load drop at peak load, a primary coating crack propagates into the underlying composite, where various toughening mechanisms (crack deflection, crack bridging, bifurcation and micro-cracking) are activated simultaneously in the composite to resist the damage [63]. Beyond *Stage 04*, the outer SiC coating further fragments with cracks propagating further into underlying composites signifying final failure.

The corresponding failure modes at high temperature can be classified as shown in Fig. 12b: *Stage 01* - a linear region with no crack formation or load drops; *Stage 02* - first coating crack forms at peak load in the SiC outer coating with uncracked ligament bridging and crack deflection within the coating layer activated simultaneously; the majority of the cracking stays within the coating and does not yet propagate into the underlying composite; *Stage 03* - further loading leads to a connection of coating cracks and their propagation into the underlying composite. Inside the composite, crack deflection (either at the fibre bundle/matrix interface or at the fibre/matrix interface within a fibre bundle due to the built-in weak interphase), crack bridging and bifurcation act simultaneously to resist damage. It is important to note here that no

obvious fibre pull-out nor fibre fracture was observed in this study at both room temperature and 1200 °C.

It must be emphasized that these observations, with real time imaging using X-ray tomography under load at different temperatures, offer new first-hand insights into the failure processes in these composites under C-ring compression condition, which as noted above are different from the conventional wisdom of how SiC<sub>f</sub>-SiC<sub>m</sub> composites are presumed to fail [64]. For microstructural-based modelling, these different experimental observations must be considered for a faithful description of the mechanical behaviour of these critical materials for future nuclear applications.

## 5. Conclusions

The local properties and high-temperature deformation and fracture behaviour of a SiC<sub>f</sub>-SiC<sub>m</sub> nuclear cladding tube material were investigated at ambient and 1200 °C using C-ring compression loading combined with *in situ* synchrotron X-ray computed microtomography. By performing such real-time 3D imaging of the evolution of damage, failure processes and corresponding active toughening mechanisms at each loading step during these tests at both low and high temperatures, the following conclusions can be made:

1. This material has higher hoop strength and coating failure strain at 1200 °C compared to that at room temperature; this suggests room temperature tests can be potentially used as a conservative estimate of the high temperature performance.
2. The failure processes at room temperature are different from 1200 °C although in both cases, the first crack initiated in the outer SiC<sub>f</sub>-SiC<sub>m</sub> coating leading to a load drop. As the crack propagated into the underlying composite, various toughening mechanisms in the composite were activated simultaneously at both temperatures to resist damage. Crack deflection within the SiC coating, however, was only observed at 1200 °C. No obvious fibre pull-out or breakage were observed in this loading configuration. These real-time observations are critical for improving the design of SiC<sub>f</sub>-SiC<sub>m</sub> claddings for nuclear applications.
3. The local properties, in terms of modulus and hardness were measured and the results are consistent with literature with one key message being that the fibre has a lower modulus and hardness than that of the matrix.
4. The residual stresses were mapped using Raman spectroscopy and suggested a relative tensile residual stress in the outer SiC coating at RT which can be a potential factor contributing to the high failure strain at 1200 °C. The exact reason for the high failure strain of SiC coating at 1200 °C is unclear and future systematic study using transmission electron microscopy methods would be helpful here. Further work is also needed to identify the fundamental mechanisms responsible for the different fracture processes at room temperature and 1200 °C.

### Data availability

Data will be made available on request.

### Declaration of Competing Interest

The authors declare that they have no known competing financial interests or personal relationships that could have appeared to influence the work reported in this paper.

## Acknowledgements

D.L. acknowledges funding support from UK EPSRC (EP/T000368/1, EP/N004493/2). The authors also acknowledge the use of the X-ray synchrotron micro-tomography beamline (8.3.2) at the Lawrence Berkeley National Laboratory's Advanced Light Source, which is supported by the Office of Science of the U.S. Department of Energy under contract no. DE-AC02-05CH11231. Thanks are also due to Dr. Dula Parkinson for help with these synchrotron tomography experiments.

## Appendix A. Supplementary material

Supplementary data to this article can be found online at <https://doi.org/10.1016/j.matdes.2023.111784>.

## References

- [1] T. Nozawa, S. Kim, K. Ozawa, H. Tanigawa, Stress envelope of silicon carbide composites at elevated temperatures, *Fusion. Eng. Des.* 89 (7–8) (2014) 1723–1727, <https://doi.org/10.1016/j.fusengdes.2013.12.032>.
- [2] T. Koyanagi, Y. Katoh, T. Nozawa, Design and strategy for next-generation silicon carbide composites for nuclear energy, *J. Nucl. Mater.* 540 (2020) 152–375, <https://doi.org/10.1016/j.jnucmat.2020.152375>.
- [3] J. Braun, C. Sauder, Mechanical behavior of SiC/SiC composites reinforced with new Tyranno SA4 fibers: effect of interphase thickness and comparison with Tyranno SA3 and Hi-Nicalon S reinforced composites, *J. Nucl. Mater.* 558 (2022), <https://doi.org/10.1016/j.jnucmat.2021.153367>.
- [4] K. Shimoda, T. Hinoki, H. Kishimoto, A. Kohyama, Enhanced high-temperature performances of SiC/SiC composites by high densification and crystalline structure, *Compos. Sci. Technol.* 71 (3) (2011) 326–332, <https://doi.org/10.1016/j.compscitech.2010.11.026>.
- [5] J. Braun, C. Sauder, F. Rouillard, F. Balbaud-Célérier, Mechanical behavior of SiC/SiC composites after exposure in high temperature liquid sodium for Sodium Fast Reactors applications, *J. Nucl. Mater.* 546 (2021), <https://doi.org/10.1016/j.jnucmat.2020.152743>.
- [6] Y. Chen, J. Marrow, Effect of irradiation swelling on the mechanical properties of unidirectional SiC/SiC composites: a numerical investigation at microstructural level, *J. Nucl. Mater.* 569 (2022), <https://doi.org/10.1016/j.jnucmat.2022.153918>.
- [7] J.D. Arregui-Mena, T. Koyanagi, E. Cakmak, C.M. Petrie, W.J. Kim, D. Kim, C.P. Deck, C. Sauder, J. Braun, Y. Katoh, Qualitative and quantitative analysis of neutron irradiation effects in SiC/SiC composites using X-ray computed tomography, *Compos. Part. B - Eng.* 238 (2022), <https://doi.org/10.1016/j.compositesb.2022.109896>.
- [8] L.L. Snead, T. Nozawa, M. Ferraris, Y. Katoh, R. Shinavski, M. Sawan, Silicon carbide composites as fusion power reactor structural materials, *J. Nucl. Mater.* 417 (1–3) (2011) 330–339, <https://doi.org/10.1016/j.jnucmat.2011.03.005>.
- [9] T. Koyanagi, H. Wang, C.M. Petrie, C.P. Deck, W.J. Kim, D. Kim, C. Sauder, J. Braun, Y. Katoh, Thermal diffusivity and thermal conductivity of SiC composite tubes: the effects of microstructure and irradiation, *J. Nucl. Mater.* 557 (2021), <https://doi.org/10.1016/j.jnucmat.2021.153217>.
- [10] S.J. Zinkle, K.A. Terrani, J.C. Gehin, L.J. Ott, L.L. Snead, Accident tolerant fuels for LWRs: a perspective, *J. Nucl. Mater.* 448 (1–3) (2014) 374–379, <https://doi.org/10.1016/j.jnucmat.2013.12.005>.
- [11] C.P. Deck, G.M. Jacobsen, J. Sheeder, O. Gutierrez, J. Zhang, J. Stone, H.E. Khalifa, C.A. Back, Characterization of SiC-SiC composites for accident tolerant fuel cladding, *J. Nucl. Mater.* 466 (2015) 667–681, <https://doi.org/10.1016/j.jnucmat.2015.08.020>.
- [12] T. Koyanagi, Y. Katoh, T. Nozawa, L.L. Snead, S. Kondo, C.H. Henager Jr, M. Ferraris, T. Hinoki, Q. Huang, Recent progress in the development of SiC composites for nuclear fusion applications, *J. Nucl. Mater.* 511 (2018) 544–555, <https://doi.org/10.1016/j.jnucmat.2018.06.017>.
- [13] D.X. Yang, Y.C. Song, Y.X. Yu, X.F. Zhao, X.I. Ping, Fabrication of SiC fibres from yttrium-containing polycarbosilane, *N. Nonferr. Metal. Soc.* 22 (4) (2012) 879–886, [https://doi.org/10.1016/S1003-6326\(11\)61260-0](https://doi.org/10.1016/S1003-6326(11)61260-0).
- [14] Y. Katoh, K. Ozawa, C. Shih, T. Nozawa, R.J. Shinavski, A. Hasegawa, L.L. Snead, Continuous SiC fiber, CVI SiC matrix composites for nuclear applications: properties and irradiation effects, *J. Nucl. Mater.* 448 (1–3) (2014) 448–476, <https://doi.org/10.1016/j.jnucmat.2013.06.040>.
- [15] S.M. Dong, G. Chollon, C. Labrugere, M. Lahaye, A. Guette, J.L. Bruneel, M. Couzi, R. Naslain, D.L. Jiang, Characterization of nearly stoichiometric SiC ceramic fibres, *J. Mater. Sci.* 448 (1–3) (2014) 448–476, <https://doi.org/10.1023/A:1017988827616>.
- [16] R. Yao, Z. Feng, L. Chen, Y. Zhang, B. Zhang, Oxidation behavior of Hi-Nicalon SiC monofilament fibres in air and O<sub>2</sub>-H<sub>2</sub>O-Ar atmospheres, *Corros. Sci.* 57 (2012) 182–191, <https://doi.org/10.1016/j.corsci.2011.12.019>.
- [17] J. Nance, G. Subhash, B. Sankar, R. Haftka, N.H. Kim, C. Deck, S. Oswald, Measurement of residual stress in silicon carbide fibres of tubular composites using Raman spectroscopy, *Acta. Mater.* 217 (2021), <https://doi.org/10.1016/j.actamat.2021.117164>.
- [18] D. Frazer, M.D. Abad, D. Krumwiede, C.A. Back, H.E. Khalifa, C.P. Deck, P. Hosemann, Localized mechanical property assessment of SiC/SiC composite materials, *Compos. Part. A - Appl. S.* 70 (2015) 93–101, <https://doi.org/10.1016/j.compositesa.2014.11.008>.
- [19] O. Karakoc, T. Koyanagi, T. Nozawa, Y. Katoh, Fiber/matrix debonding evaluation of SiCf/SiC composites using micropillar compression technique, *Compos. Part. B - Eng.* 224 (2021), <https://doi.org/10.1016/j.compositesb.2021.109189>.
- [20] E. Buet, C. Sauder, S. Poissonnet, P. Brender, R. Gadiou, C. Vix-Guterl, Influence of chemical and physical properties of the last generation of silicon carbide fibres on the mechanical behaviour of SiC/SiC composite, *J. Eur. Ceram. Soc.* 32 (3) (2012) 547–557, <https://doi.org/10.1016/j.jeurceramsoc.2011.09.023>.
- [21] E. Novitskaya, H.E. Khalifa, O.A. Graeve, Microhardness and microstructure correlations in SiC/SiC composites, *Mater. Lett.* 213 (2018) 286–289, <https://doi.org/10.1016/j.matlet.2017.11.093>.
- [22] Y. Chen, L. Gélébart, C. Chateau, M. Bornert, A. King, C. Sauder, P. Aimedieu, Crack initiation and propagation in braided SiC/SiC composite tubes: effect of braiding angle, *J. Eur. Ceram. Soc.* 40 (13) (2020) 4403–4418, <https://doi.org/10.1016/j.jeurceramsoc.2020.04.060>.
- [23] E. Rohmer, E. Martin, C. Lorrette, Mechanical properties of SiC/SiC braided tubes for fuel cladding, *J. Nucl. Mater.* 453 (1–3) (2014) 16–21, <https://doi.org/10.1016/j.jnucmat.2014.06.035>.
- [24] K. Shapovalov, G.M. Jacobsen, L. Alva, N. Truesdale, C.P. Deck, X. Huang, Strength of SiC<sub>r</sub>-SiC<sub>m</sub> composite tube under uniaxial and multiaxial loading, *J. Nucl. Mater.* 500 (2018) 280–294, <https://doi.org/10.1016/j.jnucmat.2018.01.001>.
- [25] K. Shapovalov, G.M. Jacobsen, C. Shih, C.P. Deck, C-ring testing of nuclear grade silicon carbide composites at temperatures up to 1900°C, *J. Nucl. Mater.* 522 (2019) 184–191, <https://doi.org/10.1016/j.jnucmat.2019.04.047>.
- [26] G.M. Jacobsen, J.D. Stone, H.E. Khalifa, C.P. Deck, C.A. Back, Investigation of the C-ring test for measuring hoop tensile strength of nuclear grade ceramic composites, *J. Nucl. Mater.* 452 (1–3) (2019) 125–132, <https://doi.org/10.1016/j.jnucmat.2014.05.002>.
- [27] L. Saucedo-Mora, T. Lowe, S. Zhao, P.D. Lee, P.M. Mummery, T.J. Marrow, *In situ* observation of mechanical damage within a SiC-SiC ceramic matrix composite, *J. Nucl. Mater.* 481 (2016) 13–23, <https://doi.org/10.1016/j.jnucmat.2016.09.007>.
- [28] P. Drieux, G. Chollon, S. Jacques, G. Couégnat, S. Jouannigot, P. Weisbecker, Synthesis and characterization of monolithic CVD-SiC tubes, *J. Eur. Ceram. Soc.* 36 (8) (2016) 1873–1883, <https://doi.org/10.1016/j.jeurceramsoc.2016.02.024>.
- [29] Y. Chen, L. Gélébart, C. Chateau, M. Bornert, A. King, P. Aimedieu, C. Sauder, 3D detection and quantitative characterization of cracks in a ceramic matrix composite tube using X-ray computed tomography, *Exp. Math.* 60 (2020) 409–424, <https://doi.org/10.1007/s11340-019-00557-5>.
- [30] B.P. Croom, P. Xu, E.J. Lahoda, C.P. Deck, X. Li, Quantifying the three-dimensional damage and stress redistribution mechanisms of braided SiC/SiC composites by *in situ* volumetric digital image correlation, *Scripta. Mater.* 130 (2017) 238–241, <https://doi.org/10.1016/j.scriptamat.2016.12.021>.
- [31] Y. Chen, L. Gélébart, C. Chateau, M. Bornert, C. Sauder, A. King, Analysis of the damage initiation in a SiC/SiC composite tube from a direct comparison between large-scale numerical simulation and synchrotron X-ray micro-computed tomography, *Int. J. Solids. Struct.* 161 (2019) 111–126, <https://doi.org/10.1016/j.ijsolstr.2018.11.009>.
- [32] F. Xu, Quantitative characterization of deformation and damage process by digital volume correlation: a review, *Theor. App. Mech. Lett.* 8 (2) (2018) 83–96, <https://doi.org/10.1016/j.taml.2018.02.004>.
- [33] J.P. Forna-Kreutzer, J. Ell, H. Barnard, T.J. Pirzada, R.O. Ritchie, D. Liu, Full-field characterisation of oxide-oxide ceramic-matrix composites using X-ray computed micro-tomography and digital volume correlation under load at high temperatures, *Mater. Des.* 208 (2021), <https://doi.org/10.1016/j.matdes.2021.109899>.
- [34] C.P. Deck, H.E. Khalifa, B. Sammulu, T. Hilsabeck, C.A. Back, Fabrication of SiC-SiC composites for fuel cladding in advanced reactor designs, *Prog. Nucl. Energy.* 57 (2012) 38–45, <https://doi.org/10.1016/j.pnucene.2011.10.002>.
- [35] Instrument\_Ref, Cold mounting systems for all materialographic applications, Struers, 2020, <https://www.struers.com/en/Library#brochures>.
- [36] W.C. Oliver, G.M. Pharr, An improved technique for determining hardness and elastic modulus using load and displacement sensing indentation experiments, *J. Mater. Res.* 7 (6) (2012) 1564–1583, <https://doi.org/10.1557/JMR.1992.1564>.
- [37] P. Chai, S. Li, Y. Li, L. Liang, X. Yin, Mechanical behavior investigation of 4H-SiC single crystal at the micro-nano scale, *Micromachines-basel.* 11 (1) (2020) 102, <https://doi.org/10.3390/mi11010102>.
- [38] Z. Xiao, Y. Yang, N. Jin, S. Liu, X. Luo, B. Huang, Microstructure and thermal residual stress analysis of SiC fiber through Raman spectroscopy, *J. Raman. Spectrosc.* 44 (9) (2013) 1306–1311, <https://doi.org/10.1002/jrs.4356>.
- [39] X. Niu, H. Zhang, Z. Pei, N. Shi, C. Sun, J. Gong, Measurement of interfacial residual stress in SiC fiber reinforced Ni-Cr-Al alloy composites by Raman spectroscopy, *J. Mater. Sci. Technol.* 35 (1) (2019) 88–93, <https://doi.org/10.1016/j.jmst.2018.09.023>.
- [40] J.F. DiGregorio, T.E. Furtak, J.J. Petrovic, A technique for measuring residual stress in SiC whiskers within an alumina matrix through Raman spectroscopy, *J. Appl. Phys.* 71 (7) (1992) 3524–3531, <https://doi.org/10.1063/1.350907>.

- [41] B.L. Wing, J.W. Halloran, Microstress in the matrix of a melt-infiltrated SiC/SiC ceramic matrix composite, *J. Am. Ceram. Soc.* 100 (11) (2017) 5286–5294, <https://doi.org/10.1111/jace.15038>.
- [42] G. Gouadec, S. Karlin, P. Colomban, Raman extensometry study of NLM202® and Hi-Nicalon® SiC fibres, *Compos. Part. B - Eng.* 29 (3) (1998) 251–261, [https://doi.org/10.1016/S1359-8368\(97\)00027-9](https://doi.org/10.1016/S1359-8368(97)00027-9).
- [43] D. Liu, B. Gludovatz, H.S. Barnard, M. Kuball, R.O. Ritchie, Damage tolerance of nuclear graphite at elevated temperatures, *Nat. Commun.* 8 (1) (2017) 15942, <https://doi.org/10.1038/ncomms15942>.
- [44] H.A. Bale, A. Haboub, A.A. MacDowell, J.R. Nasiatka, D.Y. Parkinson, B.N. Cox, D. B. Marshall, R.O. Ritchie, Real-time quantitative imaging of failure events in materials under load at temperatures above 1600°C, *Nat. Mater.* 12 (1) (2013) 40–46, <https://doi.org/10.1038/nmat3497>.
- [45] T.J. Pirezada, D. Liu, J. Ell, H. Barnard, I. Šulák, M. Galano, T.J. Marrow, R.O. Ritchie, *In situ* observation of the deformation and fracture of an alumina-alumina ceramic-matrix composite at elevated temperature using X-ray computed tomography, *J. Eur. Ceram. Soc.* 41 (7) (2021) 4217–4230, <https://doi.org/10.1016/j.jeurceramsoc.2021.01.030>.
- [46] H. Barnard, D.Y. Parkinson, B. Gludovatz, A. Haboub, N. Larson, F. Zok, F. Panerai, N.N. Mansour, H. Bale, C. Acevedo, D. Liu, High temperature x-ray micro-tomography, *AIP. Conf. Proc.* 1417 (1) (2016) 5–9, <https://doi.org/10.1063/1.4952925>.
- [47] ASTM Standard C1323-26, Standard Test Method for Ultimate Strength of Advanced Ceramics with Diametrically Compressed C-Ring Specimens at Ambient Temperature, ASTM International, West Conshohocken, PA, 2016, doi: 10.1520/C1323-16.2.
- [48] T.L. Embree, A.E. Segall, Evaluation of the uniaxiality of the stress state in C-ring fracture strength specimens, *J. Test. Eval.* 32 (2) (2004) 153–160, <https://doi.org/10.1520/jte11965>.
- [49] T. Ferreira, W. Rasband, *ImageJ User Guide IJ 1* (2012) 46r.
- [50] Thermo Scientific™ Avizo™ Software 9, User's Guide, 2018.
- [51] M. Palanca, L. Cristofolini, E. Dall'Ara, M. Curto, F. Innocente, V. Danesi, G. Tozzi, Digital volume correlation can be used to estimate local strains in natural and augmented vertebrae: an organ-level study, *J. Biomech.* 49 (16) (2016) 3882–3890, <https://doi.org/10.1016/j.jbiomech.2016.10.018>.
- [52] D.S. Knight, W.B. White, Characterization of diamond films by Raman spectroscopy, *J. Mater. Res.* 4 (2) (1989) 385–393, <https://doi.org/10.1557/JMR.1989.0385>.
- [53] L.G. Cançado, K. Takai, T. Enoki, M. Endo, Y.A. Kim, H. Mizusaki, A. Jorio, L.N. Coelho, R. Magalhães-Paniago, M.A. Pimenta, General equation for the determination of the crystallite size  $l_a$  of nanographite by Raman spectroscopy, *Appl. Phys. Lett.* 88 (16) (2006), <https://doi.org/10.1063/1.2196057> 163106.
- [54] A.C. Ferrari, J. Robertson, Pimenta MA Interpretation of Raman spectra of disordered and amorphous carbon, *Phys. Rev. B.* 61 (20) (2000) 14095, <https://doi.org/10.1103/PhysRevB.61.14095>.
- [55] F. Bernachy-Barbe, L. Gélébart, M. Bornert, J. Crépin, C. Sauder, Anisotropic damage behavior of SiC/SiC composite tubes: multiaxial testing and damage characterization, *Compos. Part. A - Appl. S.* 76 (2015) 281–288, <https://doi.org/10.1016/j.compositesa.2015.04.022>.
- [56] G. Singh, S. Gonczy, C. Deck, E. Lara-Curzio, Y. Katoh, Interlaboratory round robin study on axial tensile properties of SiC-SiC CMC tubular test specimens, *Int. J. Appl. Ceram.* 15 (6) (2018) 1334–1349, <https://doi.org/10.1111/ijac.13010>.
- [57] S. Nogami, A. Hasegawa, L.L. Snead, R.H. Jones, K. Abe, Effect of He pre-implantation and neutron irradiation on mechanical properties of SiC/SiC composite, *J. Nucl. Mater.* 329 (2004) 577–581, <https://doi.org/10.1016/j.jnucmat.2004.04.121>.
- [58] D. Liu, S. Knol, J. Ell, H. Barnard, M. Davies, J.A. Vreeling, R.O. Ritchie, X-ray tomography study on the crushing strength and irradiation behaviour of dedicated tristructural isotropic nuclear fuel particles at 1000 °C, *Mater. Des.* 187 (2020), <https://doi.org/10.1016/j.matdes.2019.108382> 108382.
- [59] P. Lipetzky, G.J. Dvorak, N.S. Stoloff, Tensile properties of a SiCf/SiC composite, *Mater. Sci. Eng. A.* 216 (1–2) (1996) 11–19, [https://doi.org/10.1016/0921-5093\(96\)10381-6](https://doi.org/10.1016/0921-5093(96)10381-6).
- [60] K. Hironaka, T. Nozawa, T. Hinoki, N. Igawa, Y. Katoh, L.L. Snead, A. Kohyama, High-temperature tensile strength of near-stoichiometric SiC/SiC composites, *J. Nucl. Mater.* 307 (2002) 1093–1097, [https://doi.org/10.1016/S0022-3115\(02\)01049-8](https://doi.org/10.1016/S0022-3115(02)01049-8).
- [61] T.D. Gulden, Mechanical properties of polycrystalline  $\beta$ -SiC, *J. Am. Ceram. Soc.* 51 (11) (1969) 585–590, <https://doi.org/10.1111/j.1151-2916.1969.tb15845.x>.
- [62] J.K. Shang, R.O. Ritchie, Crack bridging by uncracked ligaments during fatigue-crack growth in SiC-reinforced aluminum-alloy composites, *Metall. Trans. A* 20 (1989) 897–908, <https://doi.org/10.1007/BF02651656>.
- [63] R.O. Ritchie, D. Liu, *Introduction to Fracture Mechanics*, Elsevier, 2021.
- [64] A.G. Evans, Perspective on the development of high-toughness ceramics, *J. Am. Ceram. Soc.* 73 (2) (1990) 187–206, <https://doi.org/10.1111/j.1151-2916.1990.tb06493.x>.